Metal Oxide Nanoparticles in Electrospun Polymers and Their Fate in Aqueous Waste Streams

by

Natalia Hoogesteijn von Reitzenstein

A Thesis Presented in Partial Fulfillment
of the Requirements for the Degree
Master of Science

Approved April 2015 by the
Graduate Supervisory Committee:

Paul Westerhoff, Chair
Pierre Herckes
Kiril Hristovski

ARIZONA STATE UNIVERSITY

May 2015

ABSTRACT

Nanotechnology is becoming increasingly present in our environment. Engineered nanoparticles (ENPs), defined as objects that measure less than 100 nanometers in at least one dimension, are being integrated into commercial products because of their small size, increased surface area, and quantum effects. These special properties have made ENPs antimicrobial agents in clothing and plastics, among other applications in industries such as pharmaceuticals, renewable energy, and prosthetics. This thesis incorporates investigations into both application of nanoparticles into polymers as well as implications of nanoparticle release into the environment. First, the integration of ENPs into polymer fibers via electrospinning was explored. Electrospinning uses an external electric field applied to a polymer solution to produce continuous fibers with large surface area and small volume, a quality which makes the fibers ideal for water and air purification purposes. Indium oxide and titanium dioxide nanoparticles were embedded in polyvinylpyrrolidone and polystyrene. Viscosity, critical voltage, and diameter of electrospun fibers were analyzed in order to determine the effects of nanoparticle integration into the polymers. Critical voltage and viscosity of solution increased at 5 wt% ENP concentration. Fiber morphology was not found to change significantly as a direct effect of ENP addition, but as an effect of increased viscosity and surface tension. These results indicate the possibility for seamless integration of ENPs into electrospun polymers. Implications of ENP release were investigated using phase distribution functional assays of nanoscale silver and silver sulfide, as well as photolysis experiments of nanoscale titanium dioxide to quantify hydroxyl radical production. Functional assays

are a means of screening the relevant importance of multiple processes in the environmental fate and transport of ENPs. Four functional assays – water-soil, water-octanol, water-wastewater sludge and water-surfactant – were used to compare concentrations of silver sulfide ENPs (Ag_2S-NP) and silver ENPs (AgNP) capped by four different coatings. The functional assays resulted in reproducible experiments which clearly showed variations between nanoparticle phase distributions; the findings may be a product of the effects of the different coatings of the ENPs used. In addition to phase distribution experiments, the production of hydroxyl radical ($HO\cdot$) by nanoscale titanium dioxide (TiO_2) under simulated solar irradiation was investigated. Hydroxyl radical are a short-lived, highly reactive species produced by solar radiation in aquatic environments that affect ecosystem function and degrades pollutants. $HO\cdot$ is produced by photolysis of TiO_2 and nitrate (NO_3^-); these two species were used in photolysis experiments to compare the relative loads of hydroxyl radical which nanoscale TiO_2 may add upon release to natural waters. Para-chlorobenzoic acid (pCBA) was used as a probe. Measured rates of pCBA oxidation in the presence of various concentrations of TiO_2 nanoparticles and NO_3^- were utilized to calculate pseudo first order rate constants. Results indicate that, on a mass concentration basis in water, TiO_2 produces hydroxyl radical steady state concentrations at 1.3 times more than the equivalent amount of NO_3^-; however, TiO_2 concentrations are generally less than one order of magnitude lower than concentrations of NO_3^-. This has implications for natural waterways as the amount of nanoscale TiO_2 released from consumer products into natural waterways increases in proportion to its use.

DEDICATION

I want to dedicate this to the baroness doctor, for pushing and supporting.

ACKNOWLEDGMENTS

I would like to express my gratitude to my advisor, Dr. Paul Westerhoff, who has provided guidance, mentorship, awkward jokes, and exotic foods from abroad.

I would like to thank my committee members, Drs. Pierre Herckes and Kiril Hristovski, for their guidance, good humor, and European chocolate.

I want to acknowledge Roswita, unconditional supporter of scientific dreams and self-taught political analyst, and Rafael, who taught me how to close my eyes and jump.

I gratefully acknowledge the use of facilities within the LeRoy Eyring Center for Solid State Science at Arizona State University.

I want to thank Dr. Yu Yang, Dr. Robert Reed, Dr. Fariya Sharif, and Tyler Harris for providing advice, sample analysis help, and electrospinner housing construction assistance.

Thanks to Anjali for innumerable coffee walks.

Thank you to Kyle for South Mountain hikes and endless support.

TABLE OF CONTENTS

Page

Page

LIST OF TABLES

Table Page

LIST OF FIGURES

Figure Page

Figure Page

Figure Page

CHAPTER 1: METAL OXIDE NANOPARTICLE INTEGRATION INTO ELECTROSPUN FIBERS FOR BENEFICIARY USE

Abstract

Electrospinning uses an external electric field applied to a polymer solution to produce continuous fibers with diameters in the sub-micron range, large surface area, and small pores relative to woven textiles. Experimental parameters such as solution composition, viscosity, and voltage have a pronounced effect on fiber morphology, and thus, on fiber applications. Critical voltage is the voltage at which a Taylor cone is produced; the Taylor cone is the origin of the charged polymer jet that is crucial for successful electrospinning. This study investigated the potential for embedding of indium oxide and titanium dioxide nanoparticles in polyvinylpyrrolidone and polystyrene using electrospinning, and observing the effects on critical voltage needed for Taylor cone formation and viscosity of solution. Critical voltage and viscosity increased with the addition of indium oxide and titanium dioxide nanoparticles at 5 wt% engineered nanoparticles (ENPs). Fiber morphology was not found to change as a direct effect of ENP addition; however the increased concentration of 5 wt% ENP to solution resulted in a viscosity and surface tension increase which caused an overall decrease in fiber diameter. Successful addition of metal oxide ENPs to electrospun fibers widely diversifies beneficial fiber applications, yet can be seamlessly integrated into standard electrospinning processes.

Introduction

Polymer fiber materials with diameters in the submicron to nanometer range have unique characteristics which have led to increasing interest in their applications as reinforcements for composite materials, filtration, soft tissue prostheses, wound dressing, cosmetics, protective clothing, sensors, and purification of air or water.[1] Electrospinning is a method of producing these fibers that is simple with the ability to manipulate various parameters in order to produce fibers with desirable characteristics.[2] Electrospinning uses an electrically charged jet of polymer solution to produce polymer filaments. It involves a high voltage power supply, a spinneret with a metal needle, a syringe pump, and a grounded collector. A polymer or polymer composite solution is pumped through the syringe tip, which is connected to the high voltage power supply and is negatively charged. Kilovolt (kV) ranges of potential, anywhere from 10-40 kV, are applied until the surface tension of the fluid droplet on the tip of the syringe is overcome by the strength of the electric field and a charged jet of fluid stretches from the syringe tip and is deposited onto the grounded collector, forming a mat of fibers with diameters in the micro- and nanometer scale. Titanium dioxide has seen a surge in use as a photocatalyst and chemical sensor in environmental engineering, photovoltaics, and optics, especially in titanium dioxide-polymer composite thin films.[3,4] Recently, doping of electrospun fibers with titanium dioxide nanoparticles for various applications has begun to be explored.[5–7] Varying weight percentages of titanium dioxide in solution has been found to affect fiber diameter in the presence of polyaniline.[8] Operating parameters such as titanium dioxide loading content, humidity, and temperature have been found to affect the physical

properties, such as strength and brittleness, of electrospun polyacrylonitrile (PAN)-titanium dioxide fibers.[9]

The synergistic effect of solution parameters and electrostatic forces dictate the structure and morphology of electrospun fibers.[10] The electrospinning process is a balance of various parameters including, but not limited to, conditions such as relative humidity, polymer weight, distance between capillary tip and collector plate, feedrate of solution, solution composition, and voltage.[11–13] For example, adjusting the relative humidity in the environment affects the number, diameter, shape, and distribution of pores on the surface of electrospun fibers.[11]

The formation of a Taylor cone is one of the main features of the electrospinning process. The Taylor cone is formed at the capillary tip when the electric field overcomes the surface tension of the droplet of polymer solution at the capillary tip. This results in an elongated jet of charged solution which emanates from the Taylor cone.[1] The charged jet is the distinguishing characteristic between electrospinning and electrospraying, where a spray of charged polymer droplets is the end result and no fiber is formed.[10] The voltage at which the jet forms is called the critical voltage. Differences in the shape of the originating droplet have been observed in relation to voltage. At lower voltages, the originating drop at the capillary tip is larger than the diameter of the capillary tip. As voltage increases, the jet originates first from the bottom of the drop, and then the drop diameter decreases with increasing voltage, until finally, the jet originates from the solution within the syringe tip.[10]

Recently, there has been increasing interest in coupling the benefits of metal oxide nanoparticles with the process of electrospinning, which affords myriad applications of economically produced, micrometer and nanometer-scale fibers.[14] This study investigated how the addition of ENPs may change the experimental parameters for optimum fiber production. Specifically, this study targeted the differences in critical voltage needed to produce an unstable and stable Taylor cone by doping two polymer solutions with different weight percentages of nanoparticles, as well as solution viscosity. Voltage was slowly increased until a stable Taylor cone was observed. Nanoparticle-polymer composite solution viscosity was tested using rheometry. Titanium dioxide nanoparticles, indium oxide nanoparticles, and electrospun polymeric fibers where characterized using transmission electron microscopy (TEM), energy dispersive X-ray analysis (EDAX), and ImageJ software.

Experimental

MATERIALS. Polymers utilized were Polyvinylpyrrolidone K90 (MW 360,000 g/mol, Fluka Analytical) and Polystyrene (MW 350,000 g/mol, Aldrich Chemistry). N,n-dimethylformamide (DMF, Sigma-Aldrich) was used as the organic solvent. Nanoparticles used for doping include indium oxide nanopowder from U.S. Research Nanomaterials, Inc., Houston, TX, and Degussa AG Aeroxide P25 titanium dioxide (Frankfurt am Main, Germany).

Indium oxide-polymer composite and titanium dioxide-polymer composite solutions were prepared by dispersing various concentrations of nanoparticles (0, 0.05, 0.5, and 5 wt%) in DMF by bath sonication (Branson 2510, Branson Ultrasonic, Dansbury, CT, USA).

Weight percentages were chosen in order to include multiple orders of magnitude. Polymer (20 wt% of either PS or PVP) was added to the solution and gently stirred for 24 hours while being heated to 40°C.

Hematite ENPs were synthesized by modifying a previously published method.[15] Anhydrous ferric acid (Sigma-Aldrich) and hydrochloric acid (EMD Chemicals Group) were used to prepare a 4 mM HCl solution and 0.25 M $FeCl_3$ stock. The 4 mM HCl stock was brought to a boil on a hot plate in an Erlenmeyer flask. Then, 500 mL of 0.25 M FeCl3 solution was pipetted into the boiling HCl in 40 mL aliquots for a final concentration of 20 mM FeCl3. The solution was then placed in a laboratory oven (HP 5890 series II) at 100°C and incubated for 10 hours. The hematite ENPs were centrifuged and washed repeatedly with nanopure water five times. After rinsing, the hematite ENPs were stored at 4°C.

Table 1.1. Nanoparticle Type and Size

Nanoparticle type	Size by TEM (nm)
TiO_2	27±7
In_2O_3	80±17
Fe_2O_3	46±3

ELECTROSPINNING. Electrospinning was performed using a high voltage power supply that provided up to 40 kV (Gamma High Voltage, Ormond Beach, FL), a syringe pump (New Era NE-300, Farmingdale, NY), a 10 mL plastic syringe, and a grounded aluminum foil coated collector which was placed 15 cm away from the syringe tip. Experimental procedure consisted of loading the solution into a plastic 10 mL syringe fitted with a stainless steel needle which was connected to the high voltage power supply. The

composite solution was injected at 20 µL/hour through a stainless steel, 22-gauge needle (Sigma-Aldrich stainless steel 304 syringe needle) onto which an alligator clip was attached to charge the needle and the polymer solution as it exited the capillary tip. The entire system was enclosed in order to mitigate the effects of air currents on the system, as well as for safety. Humidity was measured using a Xikar hygrometer. Humidity was maintained at 40% at 75°F using a sponge saturated with deionized water inside the electrospinning enclosure. All experiments were run grouped by metal oxide on the same day in quick succession to maintain ambient experimental conditions.

ANALYTICAL METHODS. Nanoparticles were characterized using a Philips CM200-FEG transmission electron microscope (see Figure 1.1 below) and a Siemens D5000 powder X-ray diffractometer (Figures 1.2 and 1.3). SEM images of fibers were obtained using a JEOL 2010F. Viscosity of polymer solutions was measured using a TA Instruments AR-G2 rheometer. Fiber diameters were measured using ImageJ software (National Institutes of Health, Washington, D.C., USA).

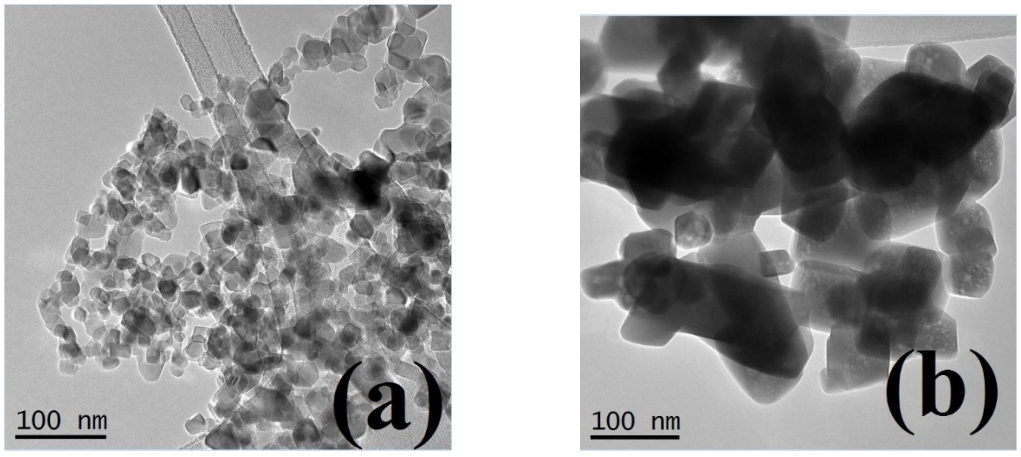

Figure 1.1. TEM Images of (A) Titanium Dioxide and (B) Indium Oxide Nanoparticles

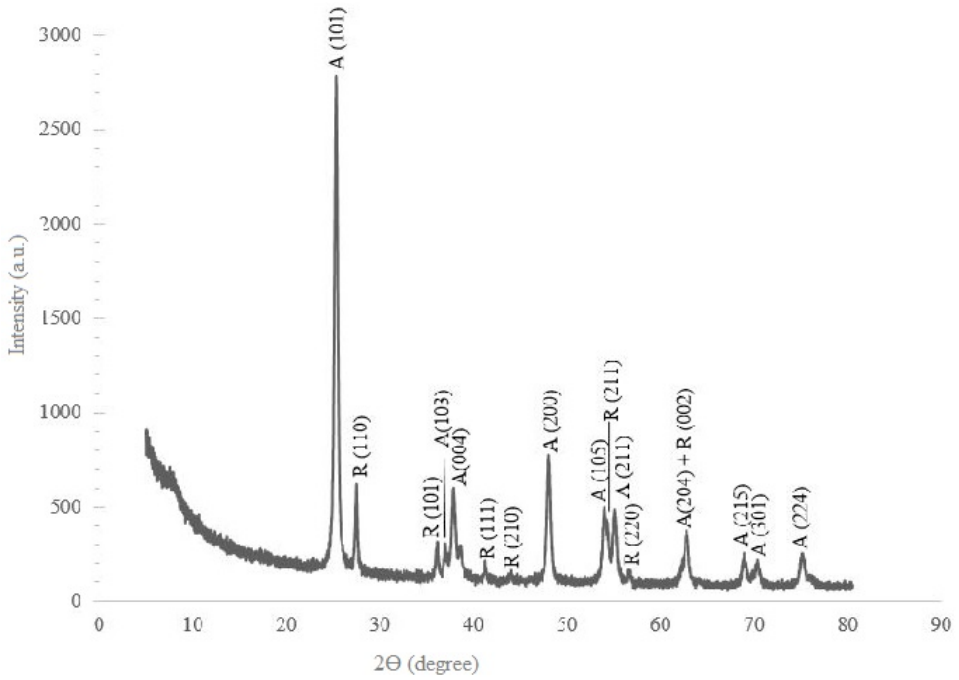

Figure 1.2. XRD Spectra of TiO_2. "A" indicates an anatase phase peak, "R" indicates a rutile phase peak

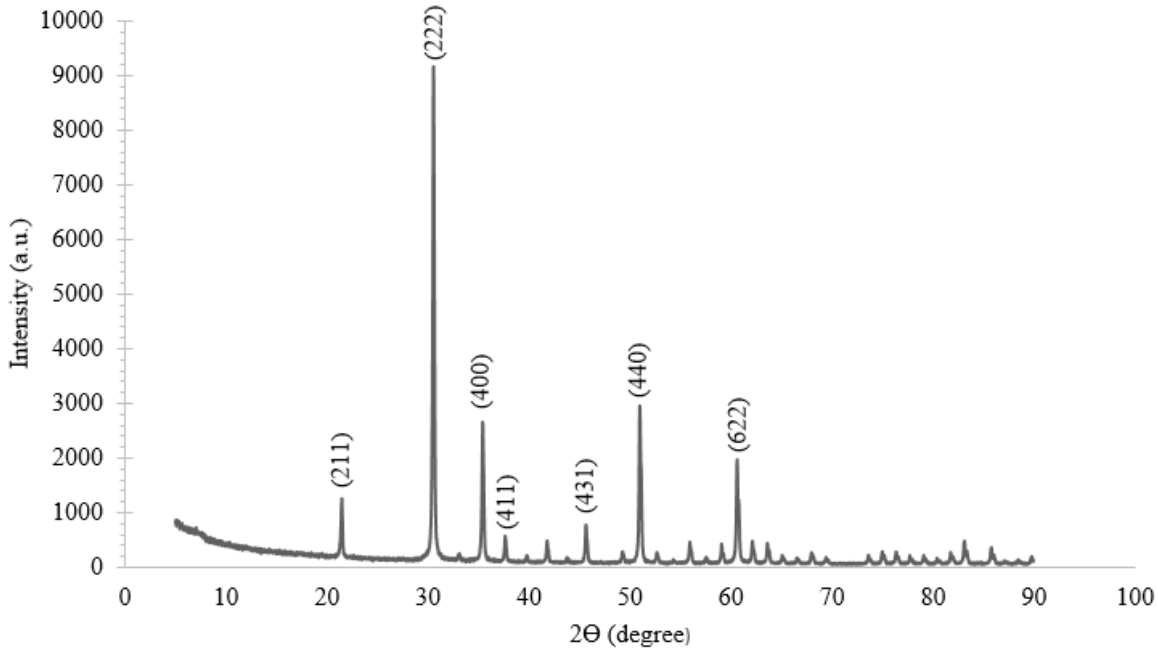

Figure 1.3. XRD Spectra of In_2O_3

Results and Discussion

1. Effect of nanoparticle doping on Critical Voltages to Produce Taylor Cones

Figures 1.4 and 1.5 show results grouped by polymer. The bars show the voltage needed to produce an unstable Taylor cone. The data within each figure is grouped by the ENP concentration as a percentage of weight (wt/wt%). Voltage needed did not vary significantly for lower weight percentages of ENPs. In the case of both PS and PVP, with 5 wt% TiO_2 and In_2O_3 added to polymer solution, the critical voltage needed to form a stable Taylor cone increased by 25% of the voltage needed to produce a cone with only polymer in solution. Significant difference in critical voltage was verified by student's t-test. P-values for these tests were 0.0023 for PVP (using a hypothetical mean of 10 kV from 0 wt% PVP tests) and 0.0008 for PS (using a hypothetical mean of 7 kV from 0 wt% ENP PS tests).

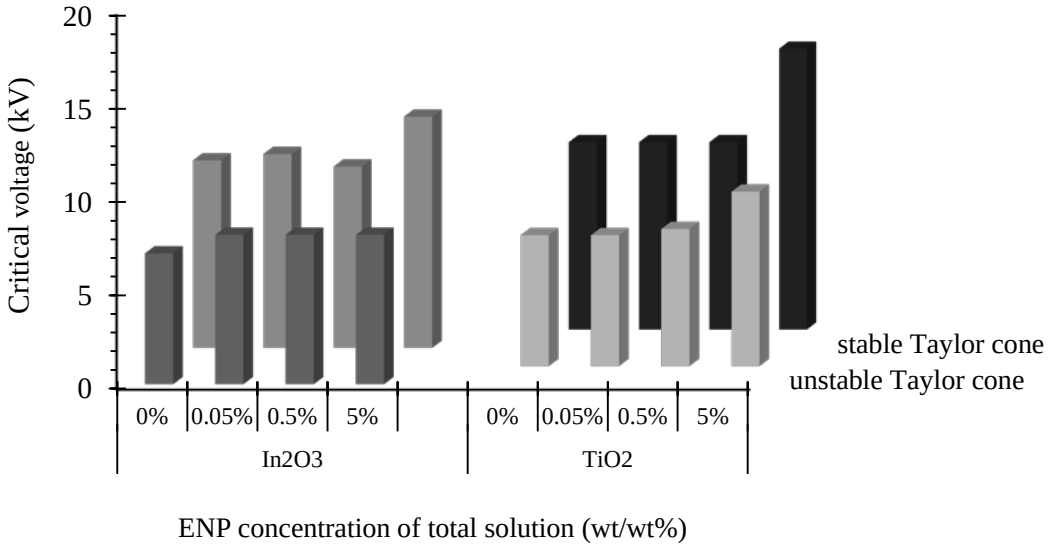

Figure 1.4. Critical Voltage to Reach Unstable and Stable Taylor Cone in PVP Solutions

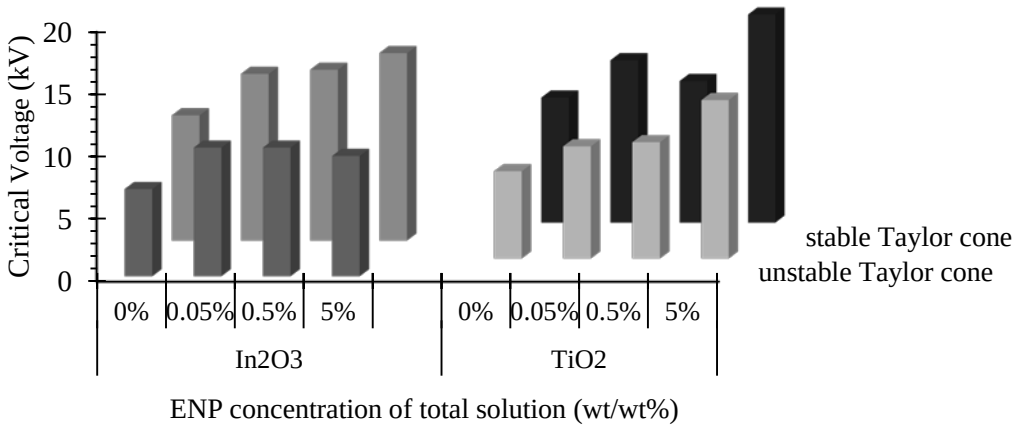

Figure 1.5. Critical Voltage to Reach Unstable and Stable Taylor Cone in PS Solutions

In order to further investigate effects of nanoparticle addition to electrospinning solutions, viscosity was measured using a rheometer. Solution viscosity plays a major role in determining the voltage needed to successfully produce a polymer jet in electrospinning, as well as affecting fiber diameter, droplet shape, and trajectory of the jet.[10,16] Figures 1.6 and 1.7 below show viscosity measurements grouped by polymer. Viscosity increased with increasing mass fraction of nanoparticles, verified by student's t-test. The increase in viscosity of the polymer solutions with 5 wt% ENP content correlates with the increase in voltage needed to produce a stable Taylor cone. Increasing viscosity increases the cohesive nature of solutions, making them harder to force through the capillary tip and increasing the instability of the Taylor cone.[10,17] The higher viscosity of the 5 wt% ENP concentration would explain the increased critical voltage needed to produce Taylor cones at higher mass fractions of nanoparticles in polymer solution.

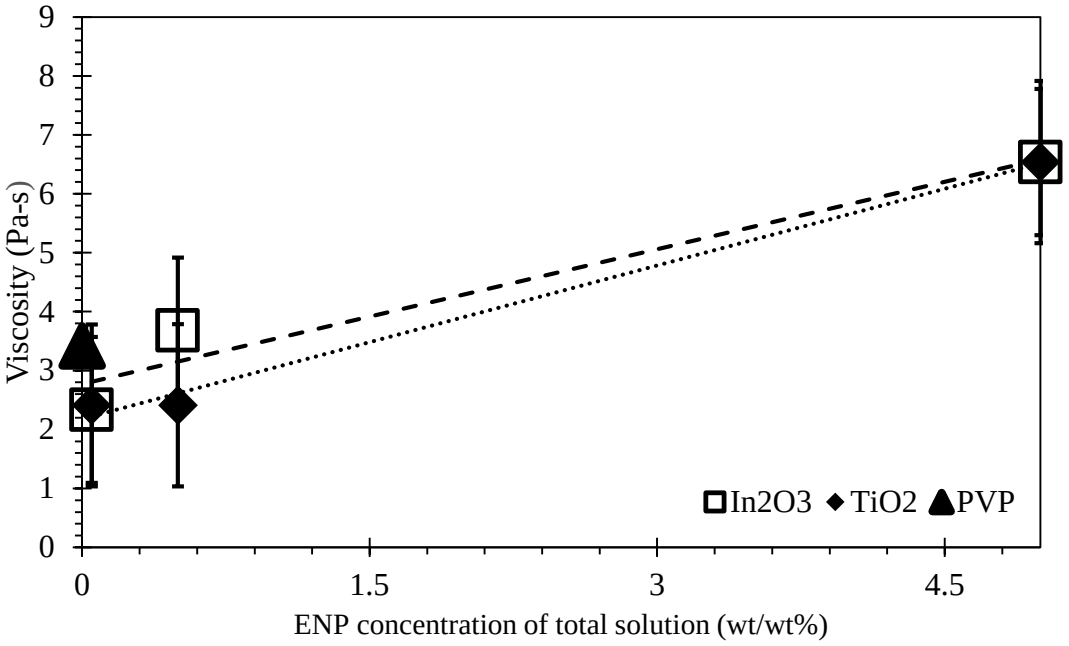

Figure 1.6. Viscosity of PVP Solutions

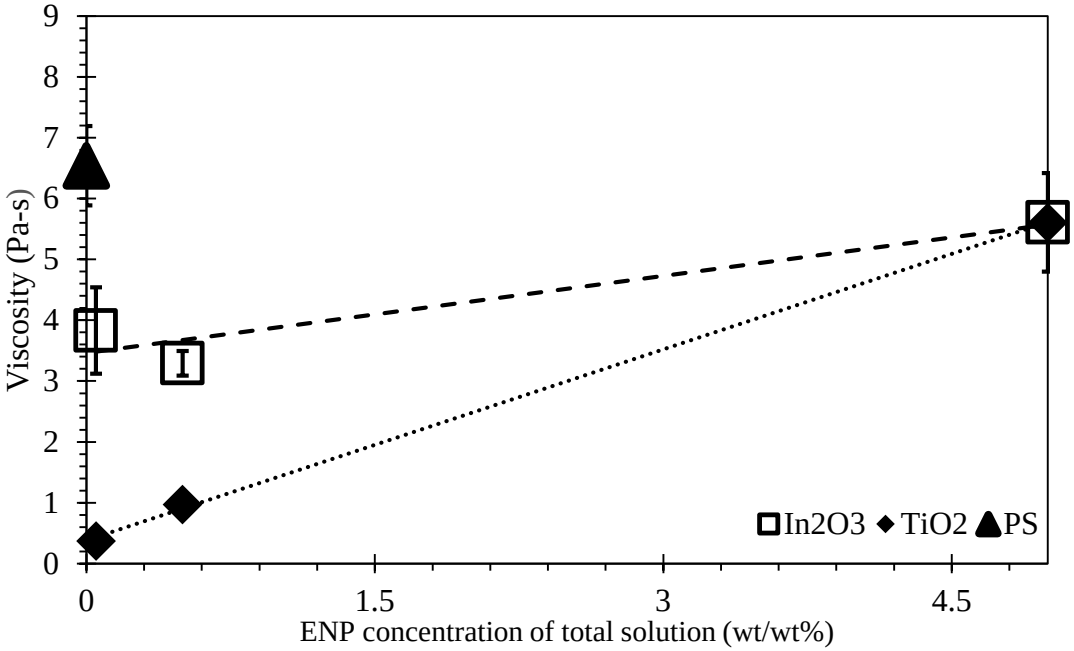

Figure 1.7. Viscosity of PS Solutions

3. Morphology of nanoparticle-polymer fibers

SEM images show differences in fiber morphology. Fibers spun with no ENPs added to solution, as shown in Figure 1.8, are smooth and show little to no beading.

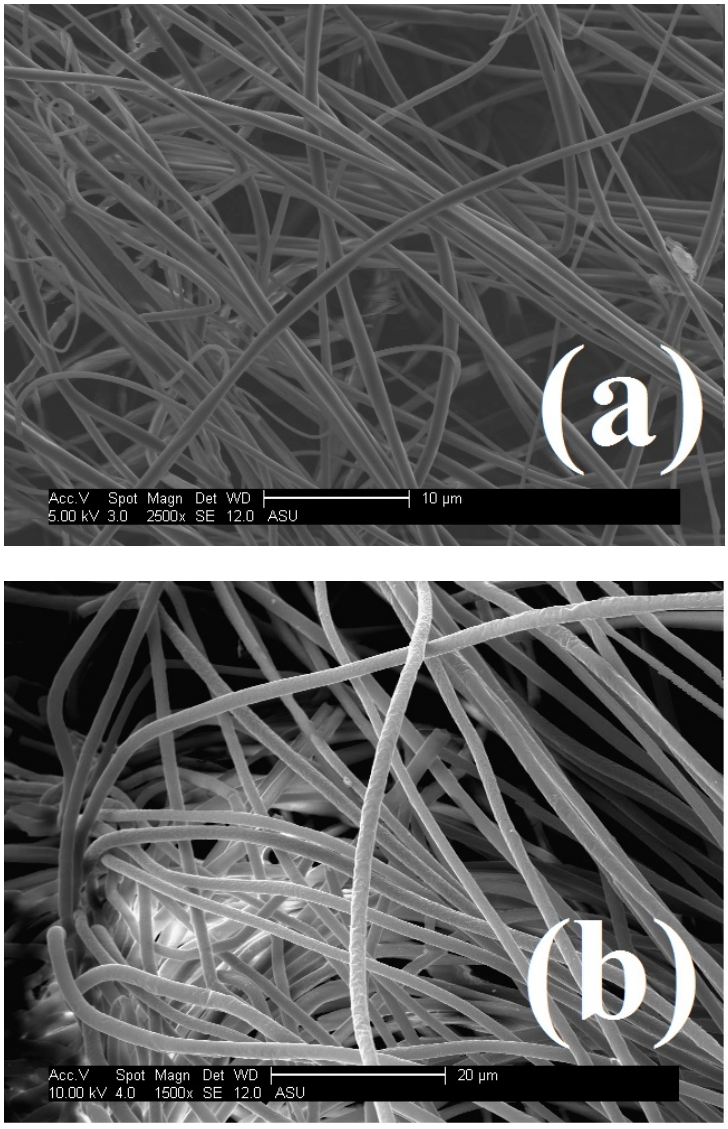

Figure 1.8. SEM Images of (A) 20 wt% PVP and (B) 20 wt% PS

Concentration and molecular weight of polymers in solution have been linked to beading and branching in electrospun fibers.[10,17,18] Figures 1.9 and 1.10 below show the

morphologies of fibers with 0.05 wt%, 0.5 wt%, and 5 wt% mass fractions of In_2O_3 and TiO_2 added. Consistent with previous studies, there are more defects in the fibers with ENPs added – beading and branching become more apparent.[11,12,19,20] Diameter of fibers did not increase between 0 wt%, 0.05 wt%, and 0.5 wt% ENP solutions; fiber diameter stayed consistent at between 1-3 μm (see table 1.2). However, with the addition of 5 wt% ENPs, diameter decreased consistently by about half (verified by student's t-test). This was caused by the increased voltage needed to obtain a Taylor cone at the higher weight percentages of ENPs. Diameter of electrospun fibers is controlled by concentration, voltage, and capillary tip diameter.[1,11,21]

Table 1.2. Diameters of Electrospun Fibers

Sample	Diameter (μm)
PS	0.81±0.20
0.05 wt% In in PS	1.9±0.43
0.5 wt% In in PS	1.8±0.52
5 wt% In in PS	0.82±0.20
0.05 wt% Ti in PS	1.45±0.53
0.5 wt% In in PS	3.8±1.8
5 wt% In in PS	0.72±0.48
PVP	1.6±0.25
0.05 wt% In in PVP	1.93±0.53
0.5 wt% In in PVP	0.59±0.15
5 wt% In in PVP	0.81±0.23
0.05 wt% Ti in PVP	1.75±0.41
0.5 wt% In in PVP	0.68±0.20
5 wt% In in PVP	0.83±0.35

Distribution of ENPs in electrospun fibers

One of the main aims of this study was to observe the distribution of ENPs in the final product. In order for nanocomposite electrospun fibers to be of use, ENPs must be accessible to chemical reagents.[22] The SEM images below (Figures 1.9 and 1.10) show ENP distributions in the various ENP concentrations used in experiments. The 5 wt%

ENP-polymer solutions show the clearest distribution of ENPs. The In_2O_3 shows the most uniform distribution, with an average of 6±2 ENP cluster/10 μm^2 area, versus 4±1 cluster/10 μm^2 area for TiO_2. The TiO_2 ENPs are about a quarter of the size of the In_2O_3 (Table 1.1) and may simply be harder to see with SEM imaging.

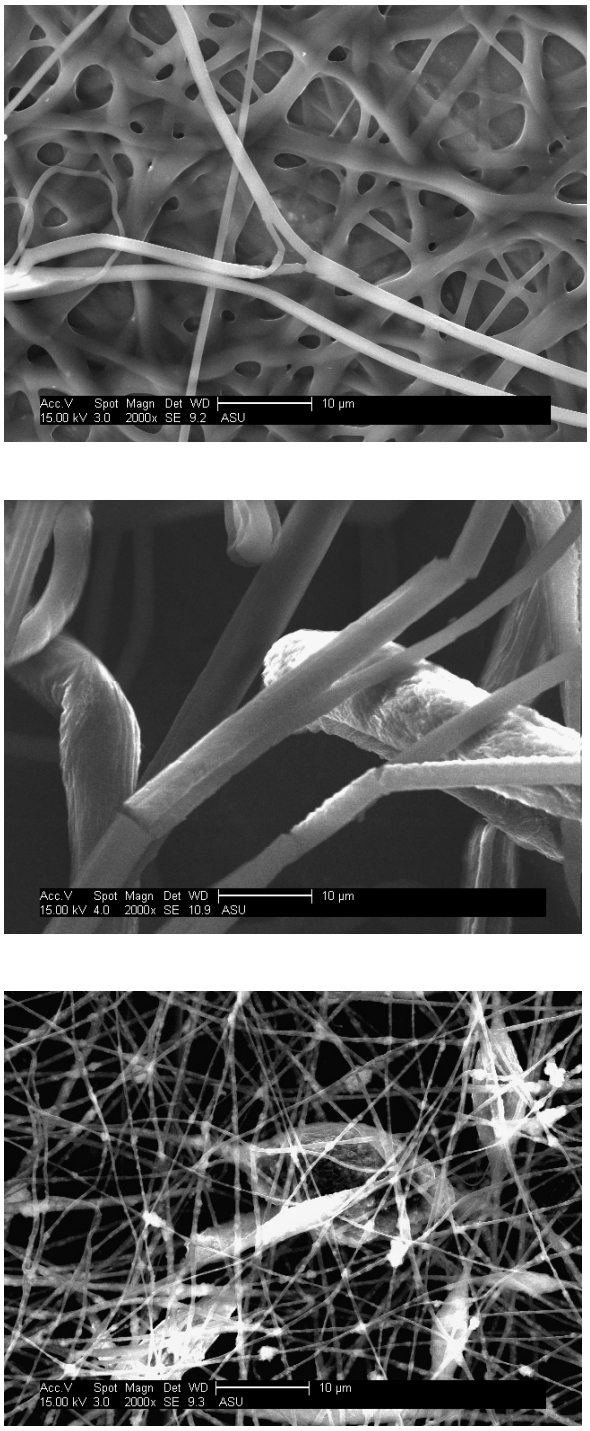

Figure 1.9. SEM Images of PS fibers with 0.05 wt% TiO_2, 0.5 wt% TiO_2, and 5 wt% TiO_2

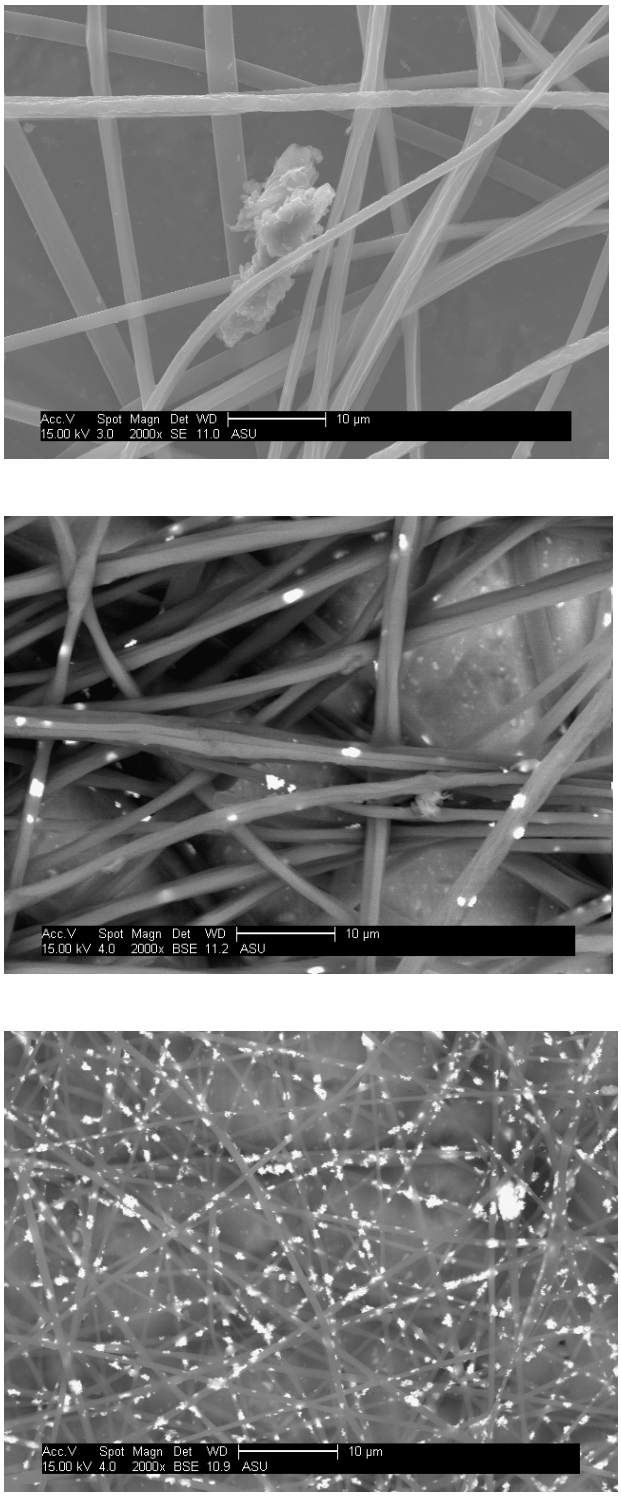

Figure 1.10. SEM Images of 0.05 wt% In_2O_3, 0.5 wt% In_2O_3, and 5 wt% In_2O_3 in PS fibers

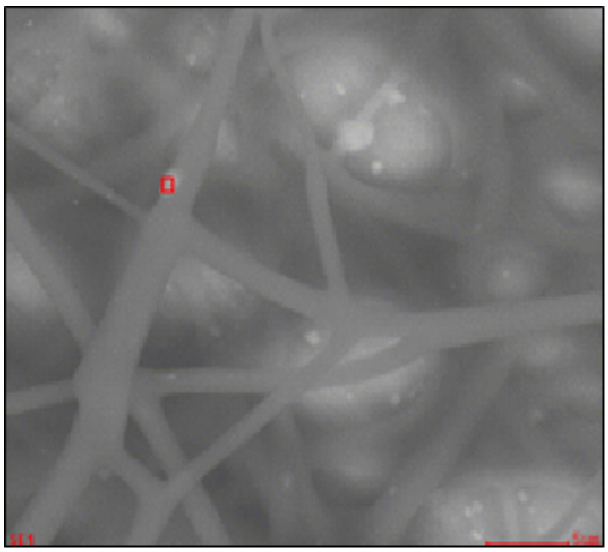

Element	Wt%	At%
AlK	54.36	67.48
SiK	02.74	03.27
InL	01.83	00.53
TiK	41.07	28.72
Matrix	Correction	ZAF

Figure 1.11. EDAX Analysis Showing TiO_2 Integration into Electrospun Fibers

Additional experiments with 1 wt% In_2O_3 were performed in order to observe fiber morphology. Figure 1.12 shows 3 wt% hematite ENPs distributed in electrospun PS fibers. Figure 1.13 below shows a puckered polymer bead in comparison to a bead of aggregated ENPs and resulting EDAX analysis of each bead. One bead is mostly polymer, while the other is a bead of aggregated ENPs.

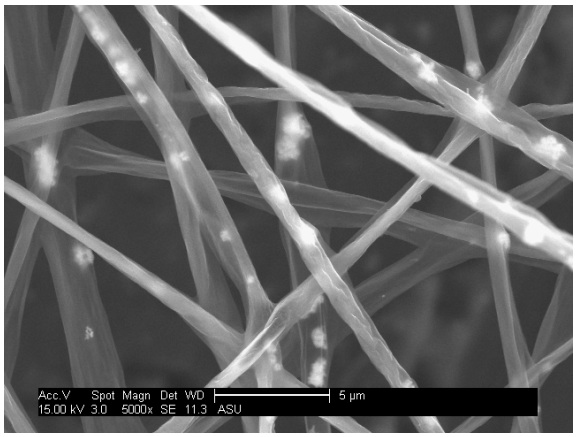

Figure 1.12. Image of 3 wt% Fe_2O_3 in PS Elemental Analysis

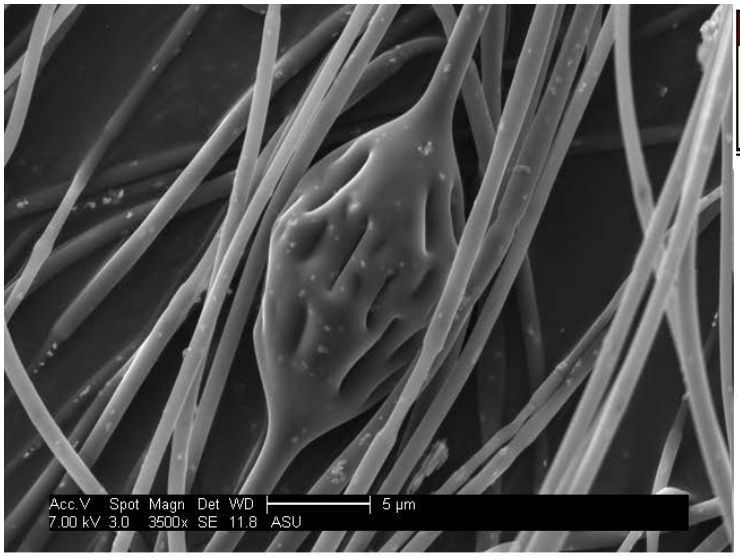

Element	Wt%	At%
CK	87.64	90.42
OK	12.36	09.58
Matrix	Correction	ZAF

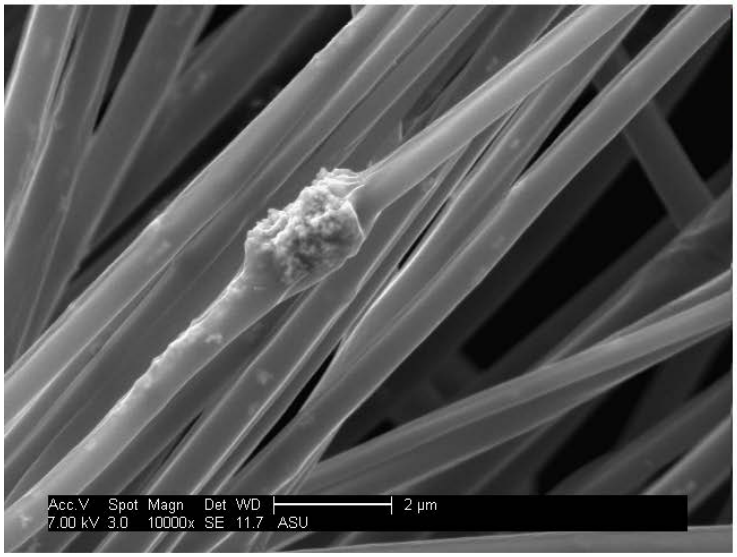

Element	Wt%	At%
CK	25.62	63.77
OK	10.48	19.59
InL	63.89	16.64
Matrix	Correction	ZAF

Figure 1.13. Images of 1 wt% In_2O_3 in PVP

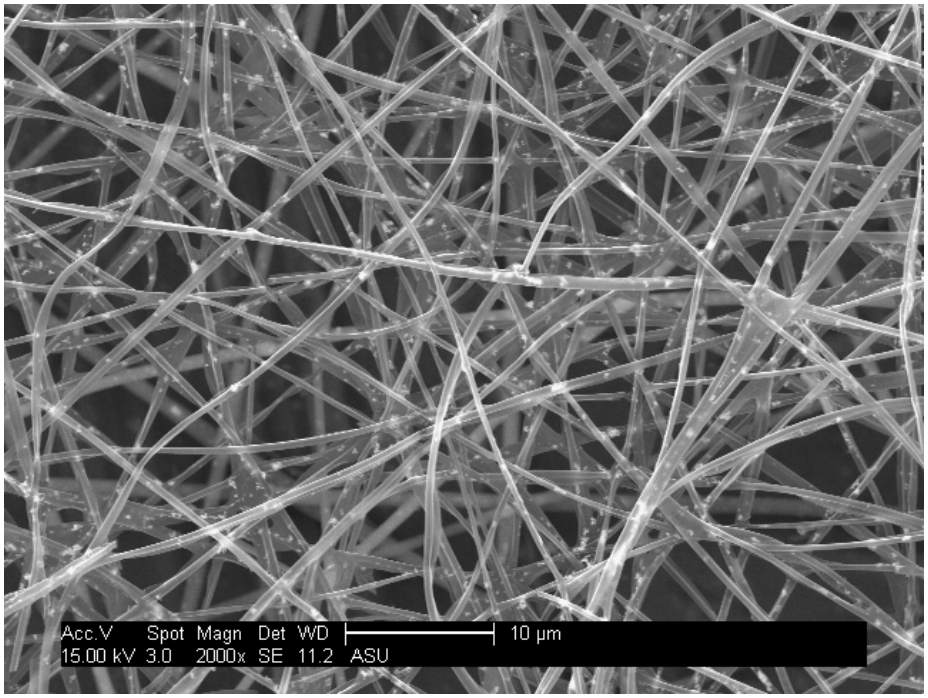

Figure 1.14. In_2O_3 NP distribution in 5 wt% In_2O_3 in PVP

Conclusion

This study investigated the effect of ENP addition to electrospun polymer fibers and how viscosity, critical voltage, and fiber morphology may change as a result. Viscosity and critical voltage were found to increase with increasing weight percentage of nanoparticles in the polymer solution. Critical voltage needed to produce a Taylor cone was also found to be higher for PS than for PVP. Fiber morphology was not found to be directly affected by ENP addition; instead the increase in viscosity and higher surface tension as a result of the 5 wt% ENP concentration caused a roughly 50% decrease in diameter. Taking higher critical voltages and viscosities into account when adding ENPs to polymer solutions has implications for future electrospinning applications. The high surface area to volume ratio of electrospun fibers coupled with nanoparticle properties may prove beneficial in a number of industries; however, special attention needs to be paid to experimental

parameters and solution composition in order to optimize fiber production. Overall, TiO_2 and In_2O_3 ENPs can be successfully integrated with into electrospun fibers with adjustments to voltage based on ENP concentration in polymer solution. High surface area, low volume, functionalization capability, and ease of synthesis all make electrospun fibers good candidates for water treatment applications such as nanofiltration and ion exchange. Further work should focus on functionalizing electrospun fibers with embedded ENPs for water treatment purposes.

CHAPTER 2: HIGH THROUGHPUT FUNCTIONAL ASSAYS TO COMPARE FUNCTIONALIZED NANOSILVER DISTRIBUTIONS BETWEEN WATER-SOIL, WATER-OCTANOL, WATER-SURFACTANT, AND WATER-WASTEWATER SLUDGE

Abstract

Functional assays are a means of screening the relevant importance of multiple processes on the environmental fate and transport of engineered nanoparticles (ENPs). Four functional assays to screen distribution of ENPs between aqueous and non-aqueous phases were evaluated: water-soil, water-octanol, water-wastewater sludge and water-surfactant. The functional assays are used to compare concentrations of silver sulfide ENPs (Ag_2S-NP) and silver ENPs (AgNP) capped by four different coatings: polyvinylpyrrolidone, citrate, and Tween 20. Water-soil experiments indicate that PVP-capped AgNPs and Ag_2S-NPs did not stay in aqueous phase. Roughly half of all ENPs stayed in the aqueous phase of the water-activated sludge experiment. For water-octanol, ENPs were found to move towards the interface of the water and octanol phases with the exception of PVP-Ag_2S-NP and Citrate-AgNP. Water-surfactant experiments showed that Tween-AgNP aqueous concentrations stay in aqueous phase with increasing concentration, while roughly half of PVP-capped ENPs stayed in aqueous solution; none of the Citrate-AgNP could be detected in the aqueous phase. Distributions vary by ENP type and functional assays, implying the functional assays are able to differentiate the role of ENP properties on net behavior of ENPs in the environment.

Introduction

Engineered nanoparticles (ENPs) are experiencing a surge in production and use in commercial products such as clothing, personal care products, pharmaceuticals, pesticides, electronics, and food.[23–26] Screening the environmental impact of ENPs through fate and transport studies necessitates information about ENP distributions in different environmental matrices, and how fate and transport are affected by ENP physico-chemical properties. ENPs may be coated with polymers or polyelectrolytes to give them desirable characteristics, and this may also affect their attachment to surfaces in terms of aggregation potential or interactions with soils and bacteria.[27–30] Silver nanoparticles in particular are in use as anti-microbial agents in consumer products, especially in clothing.[31]

Understanding how ENPs move in the environment is critical for evaluation of potential risk and exposure assessment. The environmental phase distributions of ENPs are of interest because of their release from consumer products. For example, uncoated AgNPs work by releasing silver ions (Ag^+) over time. Ag^+ is extremely toxic to bacteria, and also affects phytoplankton, invertebrates, and fish.[32,33] AgNP toxicity is heavily influenced by biodynamic and toxicity mechanisms. Whether AgNP toxicity is caused by the ENP itself or from Ag^+ release is still not well understood. Furthermore, the influence of ENP coatings has not been well studied.[34] *In vitro* and *in vivo* studies have proposed oxidative stress, mitochondrial and DNA damage, and cytokine induction as mechanisms associated with AgNP toxicity; exact mechanisms remain elusive.[35]

ENPs have distinct behaviors from other aquatic pollutants, such as organic molecules or heavy metals. Their small size (<100 nm) makes them particularly susceptible to the forces of diffusion. Studies of how viruses, bacteria, and colloids move in porous media have given researchers a base of knowledge which help explain some aspects of ENP interactions in different environmental systems.[36,37] Although ligand complexation and Derjaguin and Landau, Verwey and Overbeek (DLVO) models can help researchers to understand ENP distributions, few have been extrapolated to encompass heterogeneous environmental matrices. Extended DLVO (XDLVO), which includes magnetic and steric forces in addition to DLVO, and hydrophobic interactions have been used to explain the attachment of ENPs to porous media and hydrophobic surfaces.[30,38,39]

In order to study the phase distributions of nanoparticles in a relatively quick manner, this study sought to utilize a set of experiments that could be performed in one day as a standard procedure to test a variety of ENPs. To this end, a set of four experiments were established as a functional assay. Functional assays are investigative procedures used in laboratory studies to qualitatively assess or quantitatively measure characteristics of a target entity. To this end, high-throughput functional assays are experiments which can be performed in less than a day to determine differentiations in phase distributions of ENPs.

From the data collected via functional assays, distribution coefficients may be calculated. For example, the octanol-water distribution coefficient (K_{OW}) is a concentration ratio that describes the distribution of a contaminant between octanol and water. Octanol acts as a surrogate for organic media, such as organelles, lipid membranes, or organic matter in

soil. K_{OW} is a commonly used method for predicting transport, bioaccumulation, and toxicity of contaminants. K_d, a general designation for solid/liquid partitioning coefficient, is associated with sorption of inorganic contaminants to soils in this study. The United States Environmental Protection Agency Office of Prevention, Pesticides, and Toxic Substances (OPPTS) stipulates several methods for the study of the fate, transport, and transformation of contaminants. The sorption of substances to activated sludge biomass in wastewater treatment affects the distribution of contaminants in the environment. Non-particulate contaminants which do not sorb to biomass are not removed by clarification; they must either biodegrade, volatize, or transform in order to be removed from the system. Sorption potential data is a critical part of ENP fate and transport assesments.[40] Previous studies have evaluated the use of USEPA OPPTS 835.1110 standard method to estimate ENP removal from wastewater by comparing freeze-dried, heat-treated activated sludge as well as fresh activated sludge.[41] Cloud point extraction (CPE) is an extraction method that has been found to be highly effective; it has been shown to successfully separate AgNPs from environmental matrices with an efficiency upwards of 80% for coated AgNPs, even in complex wastewater matrices, without disturbing their size or shape.[42,43]

ENPs are often coated to make them more suitable in commercial products. ENP coatings have been found to be stable in the environment.[39] Polymer coatings, such as polyvinylpyrrolidone (PVP), may cause elastic repulsions as well as steric interactions, depending on the molecular weight, surface concentration, layer thickness, and electrokinetic potential of the coating.[39,44] Polyelectrolyte coatings of nanoscale

zerovalent iron have been shown to be slow to desorb from the metal ENPs they coat, making the ENPs remain generally more mobile in sand columns than their unmodified, uncoated counterparts.[44] When coated, the adsorbed layers of charged macromolecules give particles a combination of steric (osmotic and elastic-steric repulsion) and electrostatic repulsion. These forces are functions of charge density and concentration of the coating.[39] Surface modification of reactive nanoscale zerovalent iron has been shown to affect reactivity in water.[45] Previous studies of attachments of PVP-AgNPs and Citrate-AgNPs indicate increased attachment of PVP-AgNPs to hydrophobic surfaces in relation to Citrate-AgNPs, which showed no substantial change in attachment efficiency between hydrophilic or hydrophobic surfaces. Classic DLVO theory fell short of explaining these differences; it was postulated that hydrophobic interactions may also play a significant role.[38] The effects of coatings become important when performing risk assessment of ENPs in terms of predicting how a functionalized ENP will behave upon release from a product into the environment.

This study investigated the aqueous phase distributions of silver and silver sulfide nanoparticles coated with Tween, PVP, and citrate using a set of four functional assays developed for rapid quantitative measurements of AgNPs. The goals of this study were to verify the reproducibility of the functional assays for ENP phase distribution and to study the distribution of the AgNPs and Ag_2S-NPs to distinguish differences that may be caused by their composition.

Materials

ACS-grade Sodium bicarbonate, sodium chloride, octanol, ethylenediaminetetraacetic acid (EDTA), sodium acetate, and Triton X-114 were all purchased from Sigma-Aldrich (St. Louis, MO, USA). Sodium acetate was purchased from VWR International (Radnor, PA, USA). Elliot soil (Elliott soil bulk material, 1BS102M), classified as fine, illitic, mesic Aquic Arguidolls, was obtained from International Humic Substances Society (IHHS). Soils are very deep and poorly drained, formed in 20 inches or less of loess or silty material and silty clay loam glacial till. ENP experimental stock dispersions were prepared from as-received stock: Tween-AgNPs were acquired from Dune Sciences (Eugene, OR). PVP-AgNPs, PVP-Ag_2S-NPs, and Citrate-AgNPs were acquired from the Center for Environmental Implications of Nanotechnology at Duke University (Durham, NC).

Methods

Nanoparticle stock dispersions

Nanoparticle stock dispersion were prepared by suspending as-received nanoparticle dispersions in ultrapure water (Millipore Milli-Q, conductivity < 1.1 µS cm^{-1}). ENP experimental stock dispersions were prepared at concentrations of 5 ppm ENP in 1 mM $NaHCO_3$ buffer to maintain good dispersion. Table 2.1 summarizes ENP stock dispersions and corresponding pH.

All stock solutions were sonicated for 30 minutes in a bath sonicator (Branson 2510, Branson Ultrasonic, Dansbury, CT, USA). Particle sizes were obtained using transmission electron spectroscopy (TEM) (Philips CM-200, Eindhoven, Netherlands).

TEM sizes of at least 100 particles were measured for each of the AgNPs operated at 80 kV. Particle sizes and zeta potentials were estimated using phase-analysis light scattering (PALS) (ZetaPALS, Brookhaven Instruments, Brookhaven, NY, USA) by diluting stock solutions 20 times. Table 2.1 below summarizes the nanoparticle types and average particle sizes. DLS and electrokinetic potential measurements of experimental dispersions were made at the pH indicated in the table.

Table 2.1. Properties of Silver Nanoparticles

Ag nanoparticle type	TEM diameter (nm)	DLS diameter (nm)	Electrokinetic potential (mV)	pH of experimental dispersion
TWEEN-AgNP	20±7	63±4	-2.1±4	7.9
PVP-AgNP	38±6	91±1	-1.6±6	6.5
PVP-Ag_2SNP	48±6	63±1	-8.1±8	7.8
Citrate-AgNP	28±6	32±1	-4±4	7.9

Water-octanol distribution experiments

Experiments were conducted in pre-cleaned, EPA-certified 40 mL vials using Teflon-lined septa. First, 20 mL of octanol were added to 20 mL of ENP stock solution diluted to 1-10 mg ENP/L in 1 mM $NaHCO_3$. Octanol and ENP dispersions were added in 20 mL volumes of each. Controls consisting of water and nanoparticles without octanol, as well as blanks of octanol and water, were also prepared. Samples were placed vertically inside a rotating table at a speed of 30 revolutions per minute for three hours secured with

rubber bands and foam. After mixing, samples were allowed to settle for an hour. The octanol was vacuumed off using a pipette to access the water phase below. 10 mL aliquots of octanol and water were reserved for nanoparticle analysis.

Water-soil distribution experiments

Pre-cleaned, EPA-certified 40 mL vials with Teflon-lined septa were used for sediment distribution experiments. First, 40 mg IHHS sandy loam (Elliott soil bulk material, 1BS102M, see Materials section above for more information) was dried and weighed out into each vial. 40 mL of ENP stock solution in 1 mM $NaHCO_3$ buffer was added to each vial. Controls consisting of water and nanoparticles, as well as blanks of sediment and water, were also prepared. Samples were placed inside a rotating table at a speed of 30 revolutions per minute for three hours. After one hour of sediment settling, 10 mL aliquots of supernatant were reserved for analysis.

Water-wastewater sludge distribution experiments

Activated sludge free of nanoparticles was collected from a lab-scale biological sequencing batch reactor. The feed solution consisted of L-Glutamic acid monosodium salt monohydrate, glucose, sodium monophosphate, magnesium chloride, and sodium bicarbonate with an aeration occurring once per day, 10 hours overnight. Prior to use, the settled biomass was washed in a solution composed of 10 mM NaCl and 4 mM $NaHCO_3$ and resuspended in 1 mM $NaHCO_3$ solution stored at 4°C. Total Suspended Solids was measured by standard methods and correlated with OD720.

Immediately before the experiment, activated sludge was centrifuged at 5000g for 15 minutes and the supernatant was decanted. 40 mL 1-10 mg ENP/L solution was added to sludge in pre-cleaned, EPA-certified 40 mL vials with Teflon-lined septa. Controls consisting of water and nanoparticles without activated sludge, as well as blanks of activated sludge and water, were also prepared Samples were placed on a rotating table at a speed of 30 revolutions per minute for three hours. After gentle centrifugation at 150 g for 15 minutes followed by one hour of sediment settling, 10 mL aliquots of supernatant were reserved for analysis.

Cloud point extraction (CPE) experiments

CPE experiments were conducted using a previously published method.[42] First, 200 µL of 1.25 M sodium acetate solution, 50 µL of 1 M acetic acid, 500 µL of saturated EDTA solution, and 500 µL of 10% TX-114 was added to 40 mL of ENP stock dispersion in 1 mM $NaHCO_3$. The mixtures were shaken intensively and placed in a hot water bath at 40°C for 30 minutes. Controls consisting of water and nanoparticles without the surfactant mixture, as well as blanks of surfactant mixture and water, were also prepared Samples were than centrifuged at 5000 rpm for 12 minutes, and then allowed to cool to 0°C. After phase separation, a 10 mL aliquot of supernatant was reserved for analysis. The photo in figure 2.1 shows the final phases of the CPE experiment. The surfactant-rich phase is concentrated at the bottom after centrifugation, while the aqueous supernatant cam be clearly distinguished by the naked eye. The dark spots in the surfactant phase are ENPs that have concentrated in the surfactant-rich phase. For comparison, the leftmost sample is the blank free of ENPs.

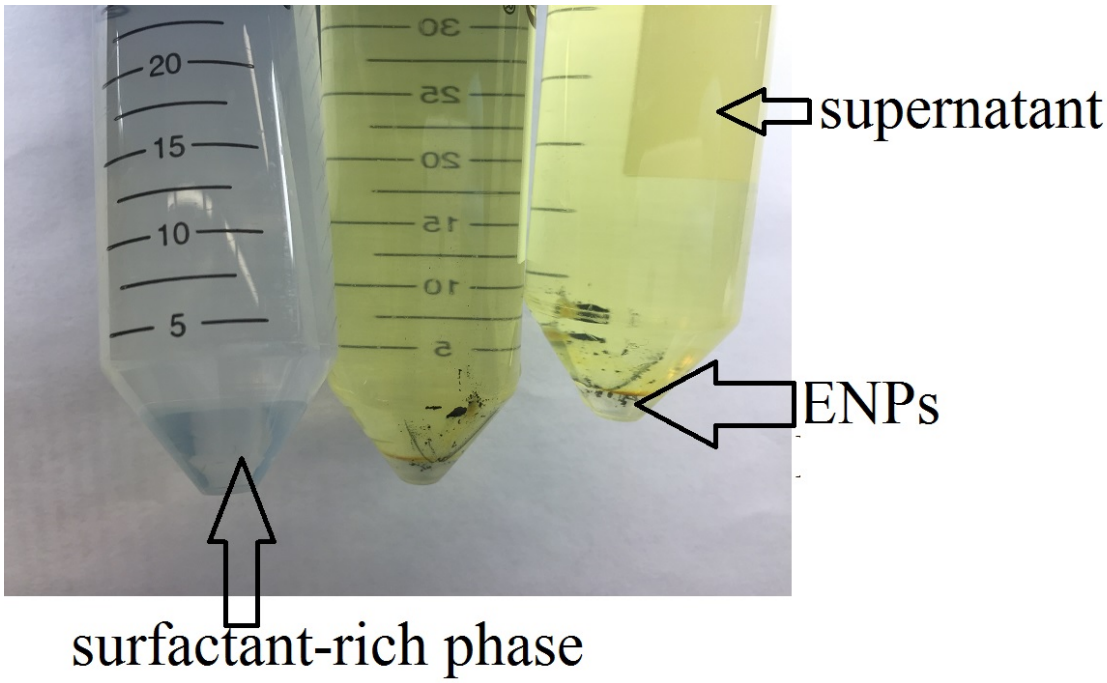

Figure 2.1. Photo of CPE End Phases

Nanoparticle quantification

Nanoparticle concentrations were quantified using UV-Vis spectroscopy. Adsorption wavelengths of 415 nm were selected for TWEEN-AgNP and PVP-AgNP, 277 nm for PVP-Ag_2S, and 401 nm for Citrate-AgNP after performing a wavelength scan and recording their entire UV-VIS adsorption spectra (see Appendix).

Results and Discussion

1. Fractional Removal of ENPs in functional assays

Water-soil distribution functional assay

In the case of soil experiments, surface charge of the AgNP as well as physico-chemical traits of the soil determine AgNP mobility in that soil. Figure 2.3 shows the percentage of

ENP remaining in the liquid phase after the functional assay. Error bars show one standard deviation. The Y-axis shows the percentage of ENP detected in the aqueous phase during analysis; C_0 is the original ENP stock dispersion concentration (i.e., 1-5 mg ENP/L, as the case may be). About 80% of the ENP concentration stayed in the supernatant for all concentrations of Tween-AgNP and Citrate-AgNP. In contrast, nearly all of the PVP-AgNP and PVP-Ag_2S-NP were associated with sediment at the end of the experiment. Soil properties such as clay content, organics content, and surface charge of soil particles all play a role in AgNP fate.[31] Most natural soil minerals are negatively charged; this means that there is a high energy barrier for AgNP attachment.[24,46,47] AgNP soil transport experiments have shown that AgNPs remain relatively mobile in natural soils.[48] PVP-AgNP mobility studies in natural soil columns found low mobility of these particular ENPs due to interaction with soil colloids, as well as favorable deposition of negatively charged PVP-AgNPs onto positively charged aluminum; straining of PVP-AgNPs credited to heteroaggregation.[49] Although all of the nanoparticles used in this study were found to have negative electrokinetic potential (Table 2.1), the citrate- and Tween-AgNPs remained in aqueous phase, which correlates with a negative electrokinetic potential; the PVP-coated Ag and Ag_2S ENPs were not detected in the aqueous phase upon analysis; this may be due to its large size, as it was the largest measured by TEM. The Ag_2S ENPs had the most negative electrokinetic potential; they should have been repulsed by the soil and should have been detected in aqueous phase. They may have settled to the bottom of the sample vial along with the soil, thereby avoiding detection in the aqueous phase.

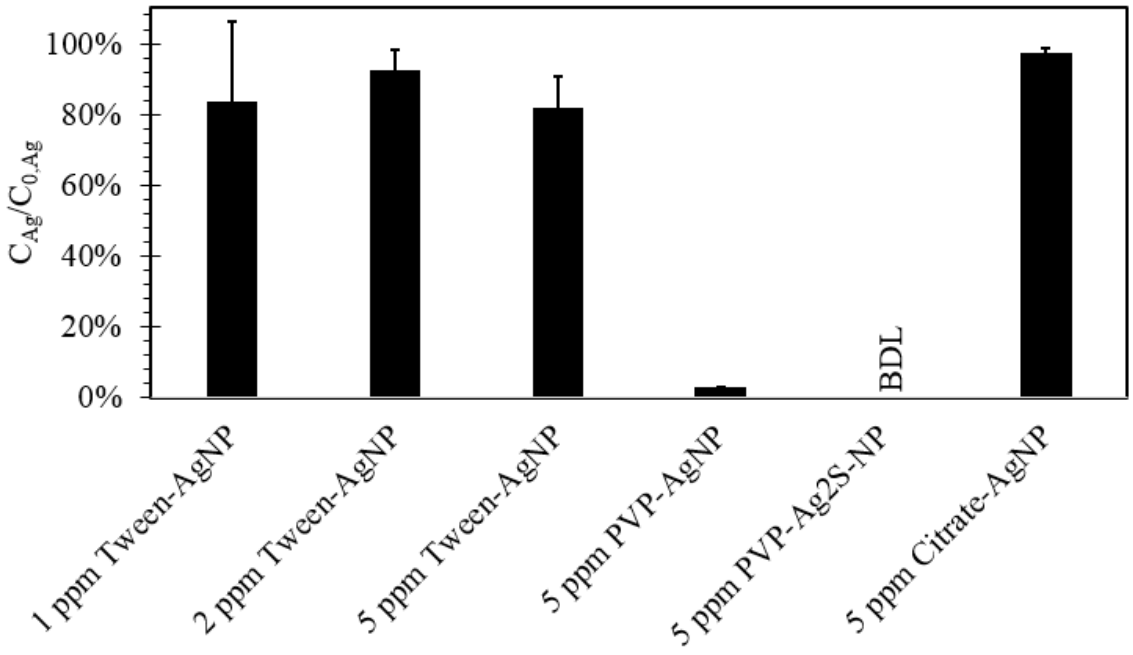

Figure 2.2. ENP Distribution in the Aqueous Phase of Water-Soil Functional Assay

Water-wastewater sludge distribution functional assay

Metallic nanomaterials have been shown to dissolve, settle, or sorb to biomass in municipal wastewater treatment plants (WWTP).[50,51] AgNPs stabilized with polyoxyethylene fatty acid ester were found to sorb to wastewater biosolids. However, there is a paucity of research on the effect of surface coating on AgNP behavior in WWTPs.[51] This study found that there was a significant fraction of AgNPs that remained in aqueous solution after three hours of exposure to biomass. Percentages of AgNPs that remained in aqueous solution were consistently around 50%, with the exception of PVP-Ag_2S (see Figure 2.2; one standard deviation is represented by the error bar). About half of the citrate-AgNP was removed from aqueous phase, which has been observed in previous studies of ENP sorption to biomass.[52]

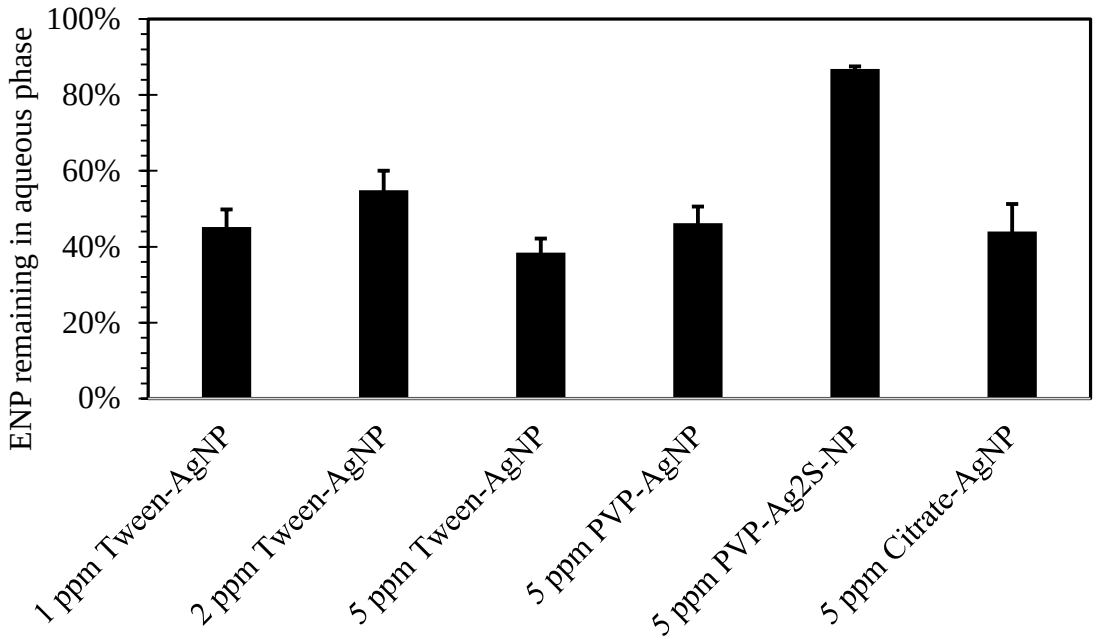

Figure 2.3. ENP Distribution in the Aqueous Phase of Water-Wastewater Sludge Functional Assay

Water-octanol distribution functional assay

Octanol-water distribution studies of coated silver, hematite, and fullerene ENPs have shown that particle surface charge, surface functionalization, and composition can have an impact on the distribution of ENPs. Around pH 8, within the pH range of natural waters and the pH range of 6.5-8.5 in this study, AgNPs were observed to distribute into the interface between octanol and water.[53] Figure 2.4 shows 5 samples; the sample furthest on the left is the ENP-free blank for comparison. The yellow tint in the octanol phase shown in the photo is ENP solution of 5 mg Tween-Ag/L. The interface between water and octanol can be distinguished by the bright yellow color of the Tween-AgNP solution. In the photo shown, AgNPs stayed in octanol phase, with significant concentration at the interface.

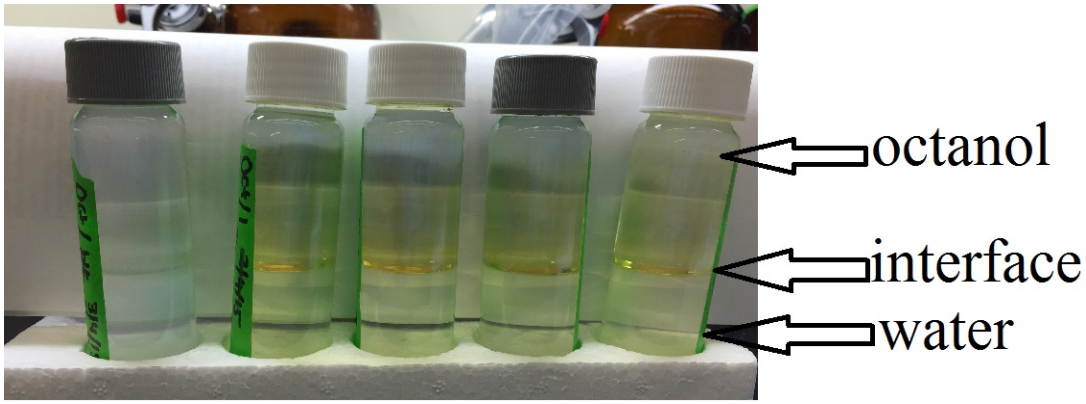

Figure 2.4. AgNP Distribution at the Water-Octanol Interface

Tween-AgNPs and PVP-AgNPs were observed to go into the interface (Figure 2.6; standard deviation is represented by the error bar). This was verified with UV-Vis analysis, where levels of ENPs detected in aqueous and octanol phases were low. Interestingly, PVP-Ag_2S and citrate-AgNPs did not follow this pattern. One possible explanation for the interface distribution could be thickness of electric double layer that surface charge is imposing a high energy barrier and therefore preventing Tween-AgNPs and PVP-AgNPs from partitioning into either aqueous or octanol phases. This could be telling of the effect of surface coating on ENP behavior.

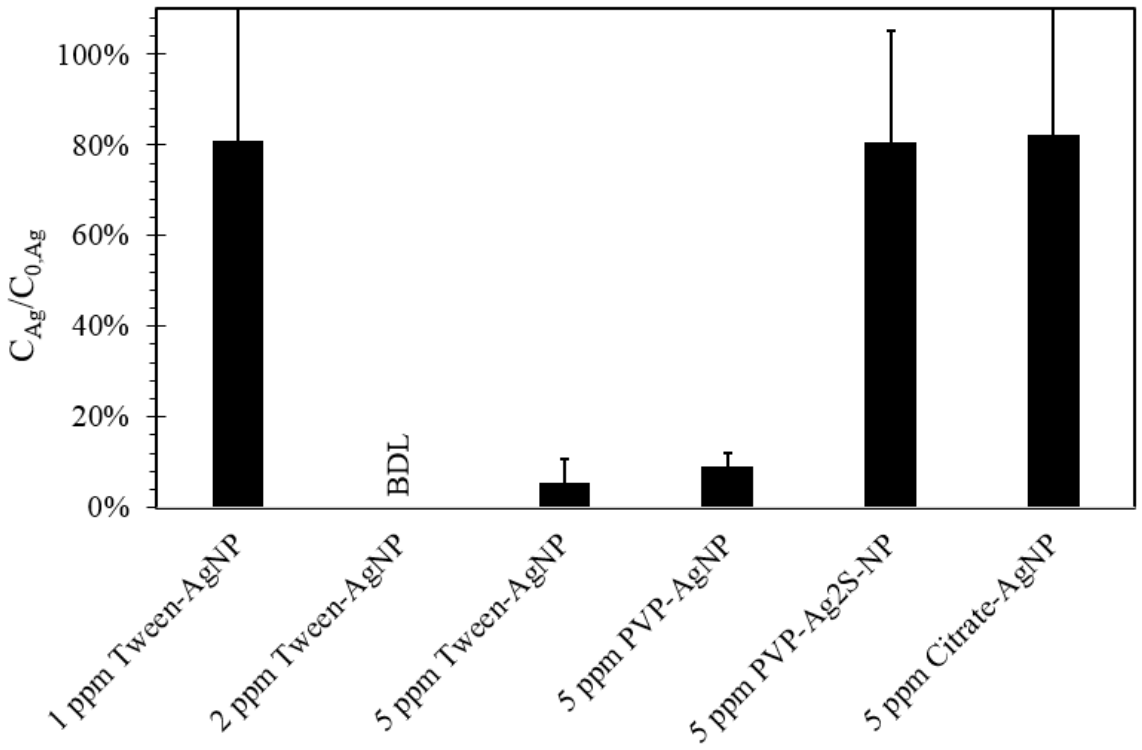

Figure 2.5. ENP Distribution in the Aqueous Phase of Water-Octanol Functional Assay

Surfactant-water distribution functional assay

In this study, roughly half of the AgNPs remained in aqueous solution with the exception of PVP-AgNP and citrate-AgNP (Figure 2.7; standard deviation is represented by the error bar). Concentration of Tween-AgNP in aqueous solution seems to increase with Tween-AgNP stock dispersion concentration. More than 90% of the original PVP-AgNP concentration remained in solution, while citrate-AgNP concentration was below detection limit. PVP-AgNPs have been classified in other studies as “soft” particles due to their thick coating with a high molecular weight polymer while Citrate-AgNPs have been classified as “hard” due to their small size, making citrate-AgNPs relatively less

hydrophobic than PVP-AgNPs and more soluble than PVP-AgNPs. Carboxylic groups on citrate coatings participate in hydrogen bonding, and PVP is a water soluble polymer.

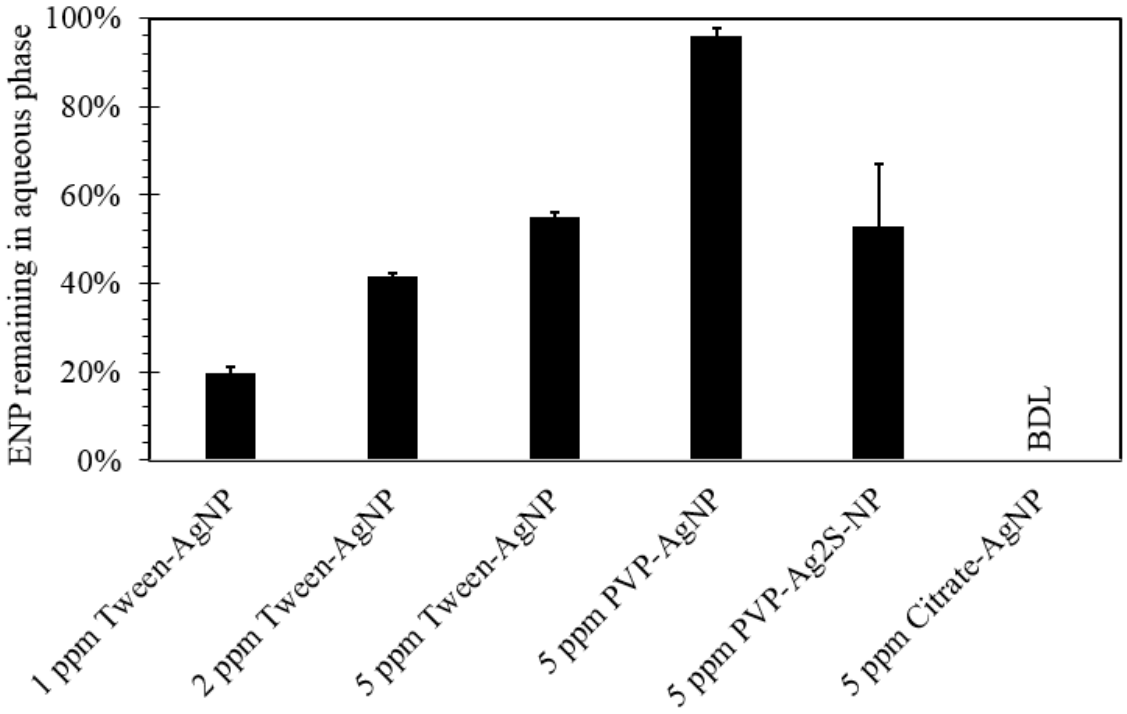

Figure 2.6. ENP Distribution in the Aqueous Phase of Water-Surfactant Functional Assay

3. Nanoparticle distribution coefficients

Table 2.2. List of Distribution Coefficient Values for ENPs

ENP type	K_{OW}, mg/L metal in octanol phase/mg/L metal dissolved	$K_{d,Soil}$, mg/kg metal sorbed/mg/L metal dissolved	$K_{d,wws,}$ mg/kg metal sorbed/mg/L metal dissolved	$Kd_{,CPE}$, (mg /kg metal in surfactant phase/mg/L metal dissolved
1 ppm Tween-AgNP	*	0.30±0.30	1.3±0.34	0.31±0.024
2 ppm Tween-AgNP	*	0.10±0.10	0.86±0.28	0.12±0.0085
5 ppm Tween-AgNP	*	0.20±0.010	1.7±0.60	0.06±0.0029
5 ppm PVP-AgNP	*	0.20±0.00	1.2±0.30	0.003±0.00087
5 ppm PVP-Ag_2S-NP	0.4±0.2	§	9±3.4	0.073±0.035
5 ppm Citrate-AgNP	*	0.30±0.01	1.4±0.72	§

*=K calculated was negative due to concentration of ENPs at interface, §=K could not be calculated because of ENP concentration being BDL at one phase

The distribution of contaminants in octanol and water in this study is described by the ratio K_{OW}[53]:

$$K_{OW,Ag}=\frac{C_{Ag\ in\ octanol}}{C_{Ag\ dissolved}},$$

where $C_{O,Ag}$ is the concentration of Ag detected in octanol in mg Ag/L, and $C_{W,Ag}$ is the concentration of Ag detected in water in mg Ag/L.

Soil and wastewater sludge distribution coefficients were modeled using K_d. For water-soil distribution, K_d was obtained using the EPA's guidelines for soil-water partitioning coefficients via soil batch experiments:

$$K_{d,soil} = \frac{\text{sorbed metal concentration } \frac{mg}{kg}}{\text{dissolved metal concentration } \frac{mg}{L}},$$

For wastewater sludge, the K_d equation used was:

$$K_{d,wws} = \frac{\text{sorbed metal concentration in } \frac{mg}{kg}}{\text{dissolved metal concentration in } \frac{mg}{L}},$$

For water-surfactant distribution, the coefficient was determined by modifying the wastewater sludge coefficient to reflect the separation of metal by the surfactant (TX-114) in solution:

$$K_{d,CPE} = \frac{\text{metal in surfactant phase } \frac{mg}{kg}}{\text{dissolved metal concentration } \frac{mg}{L}},$$

Some K values were not reported due to ENP concentrations being below detection limit.

2. Reproducibility of functional assays

Table 2.3. Concentration-Based Coefficients of Variation for Functional Assays

NP type	Water-Octanol	Water-Soil	Water-WWS	Water-surfactant
5 ppm Tween-AgNP	1	0.02	0.2	0.02
5 ppm PVP-AgNP	1	N/A	0.2	0.02
5 ppm PVP-Ag_2S-NP	0.0	N/A	1	0.3
5 ppm Citrate-AgNP	0.01	0.01	0.3	N/A

The coefficient of variance was calculated using the following equation:

$$CV=\frac{\sigma}{\mu}$$

Where σ is the standard deviation and μ is the mean. Coefficient of variation is a measurement used to compare the standard deviations of data with different units. The higher the coefficient, the more variable the data.

Variation across ENPs and functional assays was high; this may be a product of the low concentrations of ENPs used for this study. The water-surfactant functional assay was found to be the most reproducible because it had the lowest overall coefficient of variance across all ENPs and functional assays. This functional assay has been found to perform very well in other studies; it is also the most rapid to perform.[42,43] Increasing ENP concentration would make ENPs easier to detect, especially using a method with relatively low sensibility such as UV-Vis. However, concentrations higher than 5 mg ENP/L may not represent concentrations found in natural waters.

Conclusion

The increasing presence of ENPs in the environment necessitates a rapid method of comparison of ENP distributions in different environmental matrices. This study investigated the distributions of silver and silver sulfide nanoparticles coated with Tween, citrate, and PVP utilizing water-octanol, water-soil, water-wastewater sludge, and water-surfactant functional assays. Roughly half of the ENPs tested were not removed from aqueous solution during soil and activated wastewater sludge experiments. This has implications for nanoparticle partitioning into sediments and natural organic matter in natural waterways. The effect of coating on sorption of nanoparticles to activated wastewater sludge could not be confirmed. Water-octanol experiments showed that some ENPs do not stay either in aqueous or octanol phase; rather, they stay at the interface and remain highly mobile. In the case of water-surfactant experiments, only the citrate-capped AgNPs were destabilized by the surfactant. The results of this study have made it clear that more work needs to be done to clarify the effects of coatings on the interactions of ENPs and environmental matrices upon release.

CHAPTER 3: ESTIMATING EQUIVALENT AMOUNTS OF HYDROXYL RADICAL PRODUCTION FROM PHOTOLYSIS OF NOM, NITRATE, AND TITANIUM DIOXIDE

Abstract

Reactive oxygen species (ROS) are short-lived, highly reactive molecules produced by solar radiation in aquatic environments that affect ecosystem function. One commonly produced ROS is hydroxyl radical (HO·), which is produced by photolysis of natural organic matter (NOM), titanium dioxide (TiO_2), and nitrate (NO_3^-) and is highly reactive. Para-chlorobenzoic acid (pCBA) is a well-known probe for HO·, as it is highly selective for the species and generally slow to photolyze. This study measured rates of pCBA oxidation in the presence of various concentrations of Suwannee River Fulvic Acid (SRFA), TiO_2 nanoparticles, and nitrate in order to compare rates of pCBA oxidation under simulated solar light. Rate of pCBA oxidation was found to increase with increasing concentration of titanium dioxide and nitrate. Pseudo first order rate constants were calculated to compare concentrations of TiO_2, and nitrate which will produce equivalent amounts of hydroxyl radicals. Overall, titanium dioxide concentration needs to be 1.3 times less than that of nitrate to produce the same amount of HO· under simulated solar irradiation. This is important as nanoscale titanium dioxide loads from consumer products increase in natural waterways.

Introduction

Reactive oxygen species (ROS) are oxygen-containing molecules with half-lives of nanoseconds to hours that exist in aquatic environments at pico- to micromolar concentrations. ROS affects the cycling of carbon, oxygen, sulfur, and trace metals, all of which have impacts on the functioning of natural ecosystems.[54] . HO· production has powerful implications for ecosystem function; excessive amounts of this ROS leads to oxidative stress in biological systems, but they can also beneficially oxidize algal toxins and contaminants of emerging concern. ROS species in environmental systems can be identified as singlet oxygen ($^1O_2$), superoxide (O_2^-), carbonate radical ($CO_3^{-\cdot}$), hydroperoxyl radical (HOO·), hydrogen peroxide (H_2O_2), and hydroxyl radical (HO·). ROS are a product of photolysis, electron transfer, or energy transfer reactions. They have relatively low selectivity and are known to transform dissolved organic matter (DOM) and trace organics.[55–60] ROS detection is challenging due to the short lifetimes of these molecules and the inability to directly observe their production.[54,61–63]

Reactive oxygen species (ROS) studies began with atmospheric research into smog formation, stratospheric ozone depletion, and acid rain. In 1966, Van Baalen and Marler postulated that photochemical reactions, biological processes, or atmospheric deposition contribute to the production of ROS in natural waters.

Since the 1980s, environmental scientists have used a number of probes to investigate the wide occurrence of ROS species in natural waters.[54] Criteria for the selection of ROS analysis methods include sensitivity of the method, selectivity and specificity of the method to the single ROS of interest, the production of a stable and identifiable product,

and capability to allow sufficient time for adequate measurements given the short lifetimes of ROS molecules, and the probe should be relatively inert to direct photolysis and should not initiate any photochemistry of its own.[54,61] In practice, most probes fail and secondary tests or additional probes are needed.[54]

The hydroxyl radical is the most reactive and least selective of the ROS.[54] Because it does not discriminate, it not only reacts with a wide variety of organic and inorganic compounds in the environment, but it is identifiable through the use of a number of probes. Hydroxyl radical can be produced from photolysis of nitrate and nitrite (Equation 1), transition metal complexes (M) (Equation 2), photocatalysis of TiO_2 (Equation 3) dissolved organic matter, Fenton-type reactions, as well as from the decomposition of ozone.[57,64–66]

$$NO_3^- + h\upsilon \xrightarrow{H_2O} NO_2 + OH^- + HO\cdot \quad (1)$$

$$M^n + H_2O_2 \rightarrow M^{n+1} + OH^- + HO\cdot \quad (2)$$

$$TiO_2 + h\upsilon \rightarrow e^- + H^+ \quad (3)$$

$$H^+ + H_2O \rightarrow HO\cdot + H^+$$

In freshwater, the main sink of HO· is a reaction with dissolved organic matter (DOM), which forms secondary radicals (Equations 3, 4). Carbonate-rich freshwaters can also provide sinks for HO· (Equation 5).

$$OH + DOM \rightarrow DOM\cdot + H_2O \quad (3)$$

$$OH + DOM \rightarrow HO - DOM\cdot \quad (4)$$

$$OH + CO_3^{=} \rightarrow CO_3 \ + OH^- \text{ (5)}$$

Nitrate is found in all natural water systems and is an essential nutrient for ecosystem function. It is also the primary source of HO· in natural waters.[55]

Transition-metal complexes in natural waters can react to produce ROS species, such as HO·, which have the potential to be biologically damaging. This has large implications for coastal water and freshwater systems, where transition-metal concentrations are highest.[54]

Page (2010) studied the use of terephthalate (TPA) as a probe for HO·. TPA reacts with HO· to produce hydroxyterephthalate (hTPA):

Scheme 1: Production and quenching of hydroxyl radical from fulvic acid with TPA as a probe.

$$FA + hv \xrightarrow{k_{form,FA}} HO\cdot$$

$$TPA + HO\cdot \xrightarrow{k_{rxn,TPA}} \xrightarrow{\%\ yield} hTPA$$

$$FA + HO\cdot \xrightarrow{k_{quench,FA}} products$$

TPA was chosen because of its fluorogenicity, which affords higher sensitivity and lower background interference as opposed to probes dependent on UV-visible light absorption detection. 365 nm was the major wavelength isolated for the study.

HO· is quantified through the loss or accumulation of a product.[61] Para-chlorobenzoic acid (pCBA) is a probe compound that is highly selective to HO· ($k_{HO\cdot/pCBA}$=5x10^{9}M^{-1}s^{-1})[67], making its disappearance an indirect measurement of the disappearance of this ROS.

It is easy to measure, with a low detection limit of 0.025 µM (4 µg/L) via high-performance liquid chromatography (HPLC).[62,63]

Titanium dioxide (TiO_2) nanoparticles have seen a surge in use in consumer products, industrial products, and photocatalytic processes, with an estimated yearly production of 7,800-38,000 tons in the United states alone.[68,69] TiO_2 nanoparticles can be found in toothpastes, paints, paper, cosmetics, and other products, and have been identified in surface waters and wastewater treatment plant effluents.[25,70–72] Researchers are starting to investigate the occurrence of TiO_2 in natural waters and possible consequences. Differentiating between engineered and naturally occurring TiO_2 particles in these waters remains an analytical challenge.[72] Release experiments where TiO_2-containing textiles were washed indicate releases in the 1.5 to 15 µg/L range, while measured TiO_2 levels in wastewater range from 100 to 500 µg/L.[71,73]

Given the widespread use of TiO_2 in industrial and consumer products, their presence in natural waters, and their capacity to react in natural waters with natural organic matter to produce HO·, a metric for quantifying ROS production from ENMs such as TiO_2 in these scenarios would further help researchers understand the implications of such released ENMs for ecosystem stability.

The goal of this study was to estimate equivalent amount of HO· radical produced from concentrations of Suwannee River Fulvic Acid (SRFA), TiO_2 nanoparticles, and nitrate via pCBA oxidation under simulated solar light in order to further understand the consequences of increasing releases of these compounds into our natural waterways.

Materials

Ultrapure water (Nanopure) was used to prepare all solutions. Reagent grade p-Chlorobenzoic acid, boric acid, sodium hydroxide, and sodium nitrate were obtained from Sigma-Aldrich (St. Louis, MO, USA). Aquatic NOM was IHSS Suwannee River Fulvic Acid (International Humic Substances Society, USA). SRM1898 TiO_2 nanomaterial was obtained from National Institute of Standards and Technology (Washington, DC, USA).

High performance liquid chromatography (HPLC) analysis was performed using a Waters separation module 2695 (Milford, MA, USA) with a reverse-phase analytical column (RP18) to measure pCBA. The mobile phase consisted of 55% methanol and 45% 10 nM phosphoric acid at 1 mL/min. A Waters 2996 Photodiode Array Detector set to a wavelength of 234 nm was used for detection. pH was measured with a Thermo Scientific Orion STAR A329 portable meter.

Experimental

Simulated solar sunlight experiments were conducted using 100 mL aliquots of 2.5 µM pCBA with different concentrations of NOM, NO_3^-, and TiO_2 added. The sample was placed in a thermostated and jacketed reactor with 100-mL capacity. The reactor was stirred constantly and the sample was irradiated through a quartz window on top with simulated sunlight. The simulated light was provided by a 300-W xenon arc lamp (Spectraphysics Oriel, 91160A), and the output of the arc lamp was filtered through a standardized air mass 1.5 filter (AM 1.5 Global), which yielded a spectrum representative of the solar spectrum at ground level when the sun was at a zenith angle of 48.2°, and the

lamp output power was 1325 W/m^2. Additionally, some experiments were conducted with an additional 280 nm cutoff filter in order to prevent the direct photolysis of pCBA (experiments are specified below). Experiments were run for four or six hours, with 1 mL aliquots taken every 30 minutes for HPLC analysis. pH was measured every hour for both dark control and simulated sunlight samples.

Results and Discussion

Absorption spectra for pCBA, NO_3^-, TiO_2, and NOM

UV-Vis was used to measure the absorption spectra of reagents used in this study. The results are shown below (Figures 3.1-3.4), normalized to molar absorptivity using Beer's law:

$$A = \varepsilon bc,$$

where A is absorptivity, ε is molar absorptivity in L/mol-cm, b is path length (1 cm), and c is concentration in mol/L.

pCBA photolyzes below 250 nm, which was the reason for using a 258 nm cutoff filter. All species had peaks within the UV spectrum (10-400 nm). NOM acted as an HO· sink, instead of an HO· source; this may explain why pCBA oxidation was relatively low in this study.

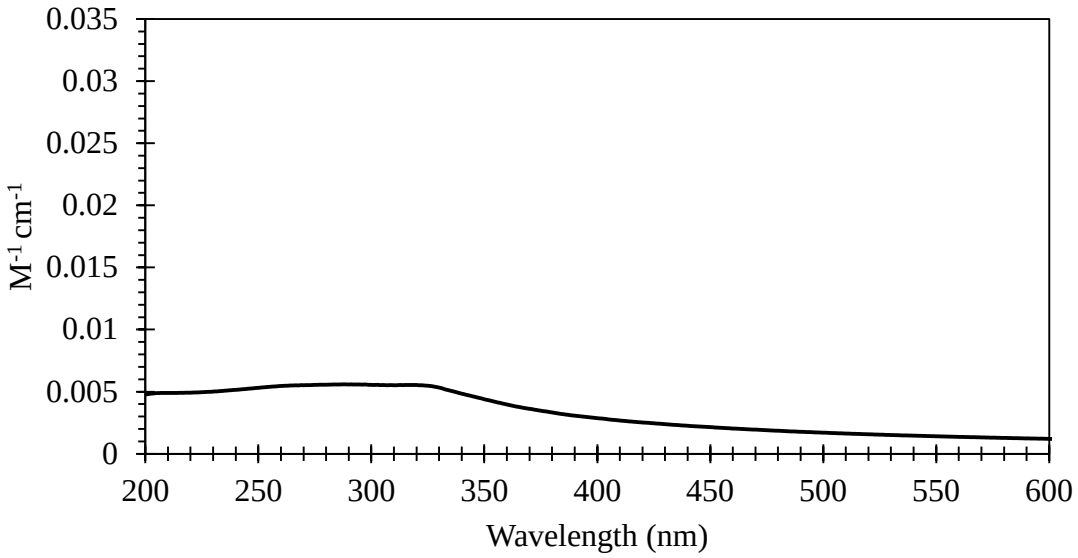

Figure 3.1 TiO_2 Absorbance Spectra Normalized to Absorptivity

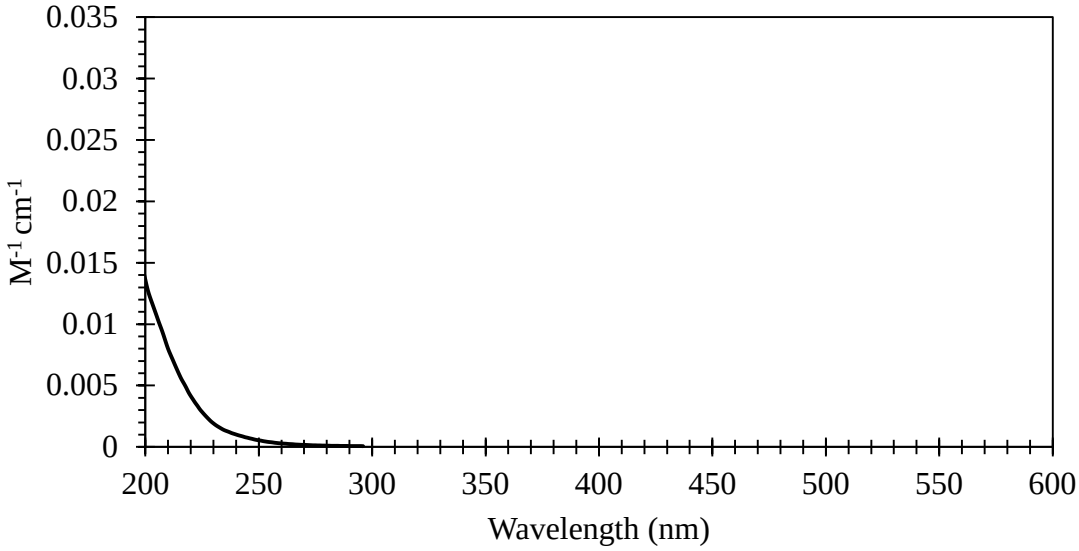

Figure 3.2. SRFA Absorbance Spectra Normalized to Absorptivity

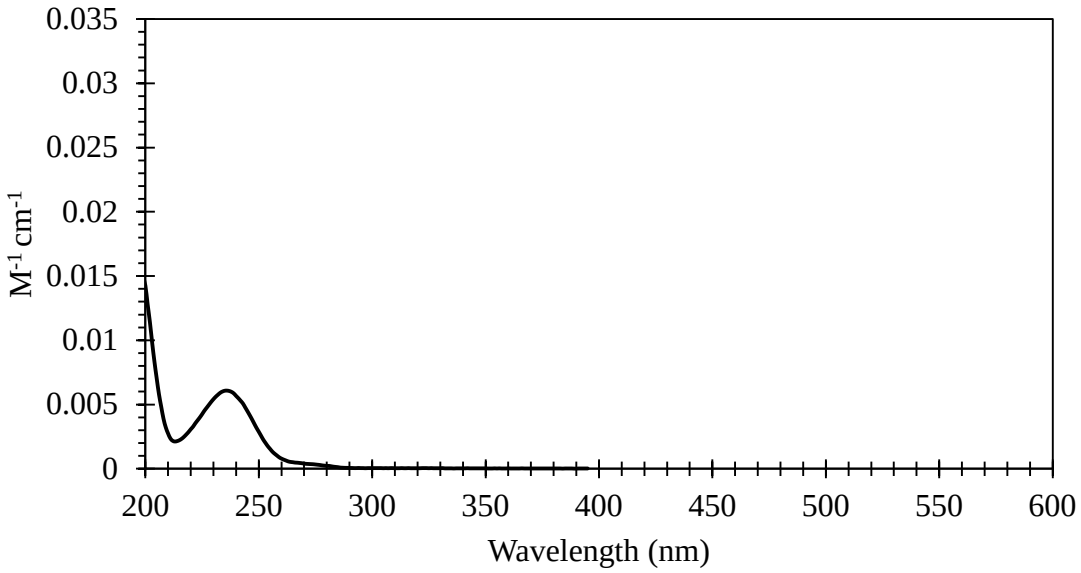

Figure 3.3. pCBA Absorbance Spectra Normalized to Absorptivity

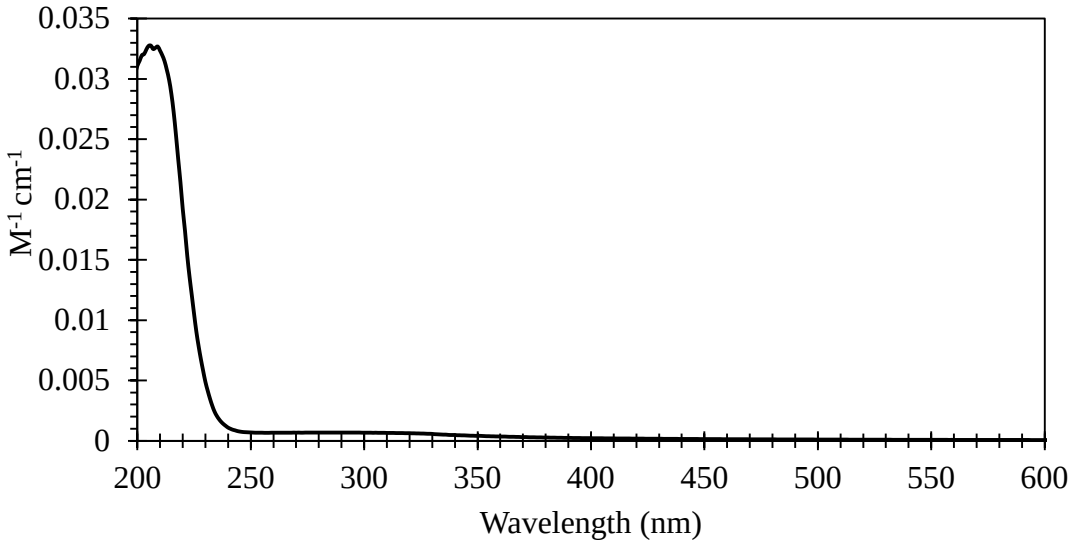

Figure 3.4. $NaNO_3$ Absorbance Spectra Normalized to Absorptivity

Changes in concentration of pCBA

Kinetic experiments were obtained using different initial concentrations of SRFA, TiO_2, and NO_3^-. The reactions are modeled as pseudo first-order:

$$\frac{d[A]}{[A]} = -k\,dt \qquad \text{(Equation 6)}$$

Upon integration, equation 6 becomes:

$$\ln\left(\frac{[A]}{[A]_0}\right) = -kt \qquad \text{(Equation 7)}$$

By fitting the data to this model, we obtain pseudo first order constants, k_{pCBA}, for the consumption of pCBA in solution over the course of several hours.

For several different concentrations of SRFA in Nanopure water under an AM 1.5 Global filter with a pH of 5, k_{pCBA} decreased with increasing SRFA concentration (Figure 3.1). Values for k_{pCBA} ranged from 0.0003 min^{-1} to 0.002 min^{-1}. The highest k_{pCBA} was for 0 ppm SRFA. NOM is a known scavenger of hydroxyl radical; in this case, the NOM may be scavenging the ROS produced in solution, exhibiting a screening effect.[57]

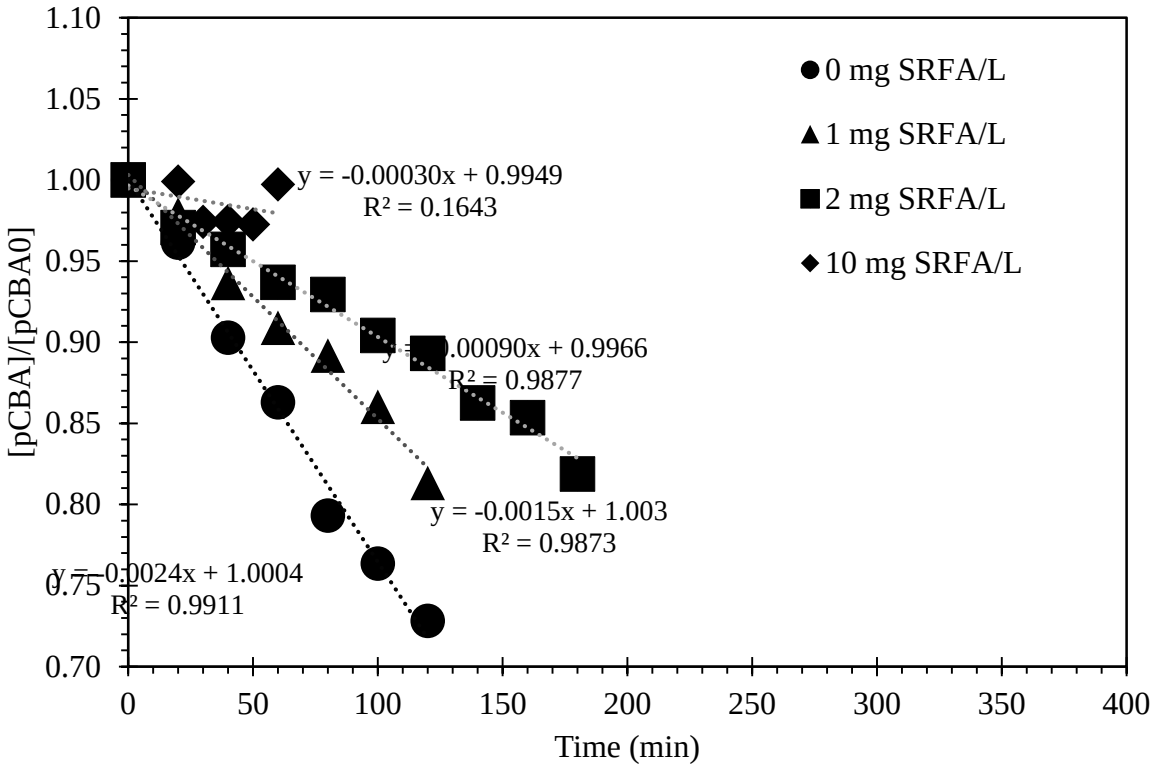

Figure 3.5. pCBA Removal in Nanopure Water with 0 ppm, 1 ppm, 2 ppm, and 10 ppm SRFA Using an AM 1.5 Global Filter

pCBA oxidation with different SRFA concentrations present in a 2.5 mM sodium bicarbonate ($NaHCO_3$) buffer at a pH of 8 (Figure 3.2). The trend in rate constants is similar to that of the SRFA in nanopure water, where increasing concentration of SRFA led to lower k_{pCBA}. Bicarbonate did not affect the reaction, with ranges for reaction rate constant similar to those in the previous figure, where no $NaHCO_3$ was used.

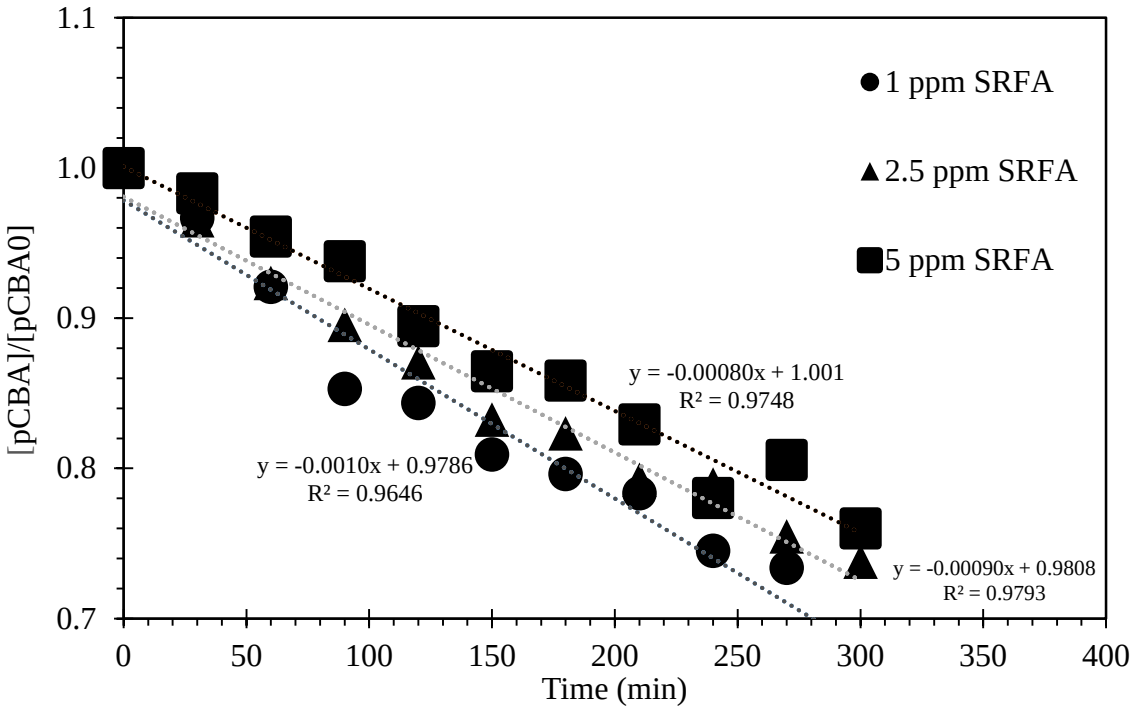

Figure 3.6. pCBA Removal in Sodium Bicarbonate with 1 ppm, 2.5 ppm, and 5 ppm SRFA Using an AM 1.5 Global Filter

Changes in pCBA concentration without NOM were measured in a matrix of Nanopure water using a 258 nm wavelength cutoff filter in addition to an AM 1.5 Global filter. The cutoff filter was added in order to prevent direct photolysis of pCBA. As shown in Figure 3.3, the rate constant for the consumption of pCBA was lower for 0.32 ppm SRFA than it was for 3 ppm SRFA; however, for 50 ppm the rate constant decreased markedly. pCBA was oxidized in the presence of TiO_2. At 0.2 ppm TiO_2, the rate constant is low and the concentration of pCBA doesn't change much over 240 minutes. In the presence of 2 ppm TiO_2, roughly 60% of the pCBA remains after 240 minutes. In the presence of 5 ppm TiO_2, about 90% of the pCBA remained after 240 minutes (see Equation 2).

The decreases in pCBA consumption at higher concentrations of both SRFA (Figure 3.3) and TiO_2 (Figure 3.4) may indicate may be a product of light scattering occurring at these

higher concentrations. The concentration of added material (TiO_2 or SRFA) may be high enough to block the light, exerting a screening effect and therefore interfering with photolysis.

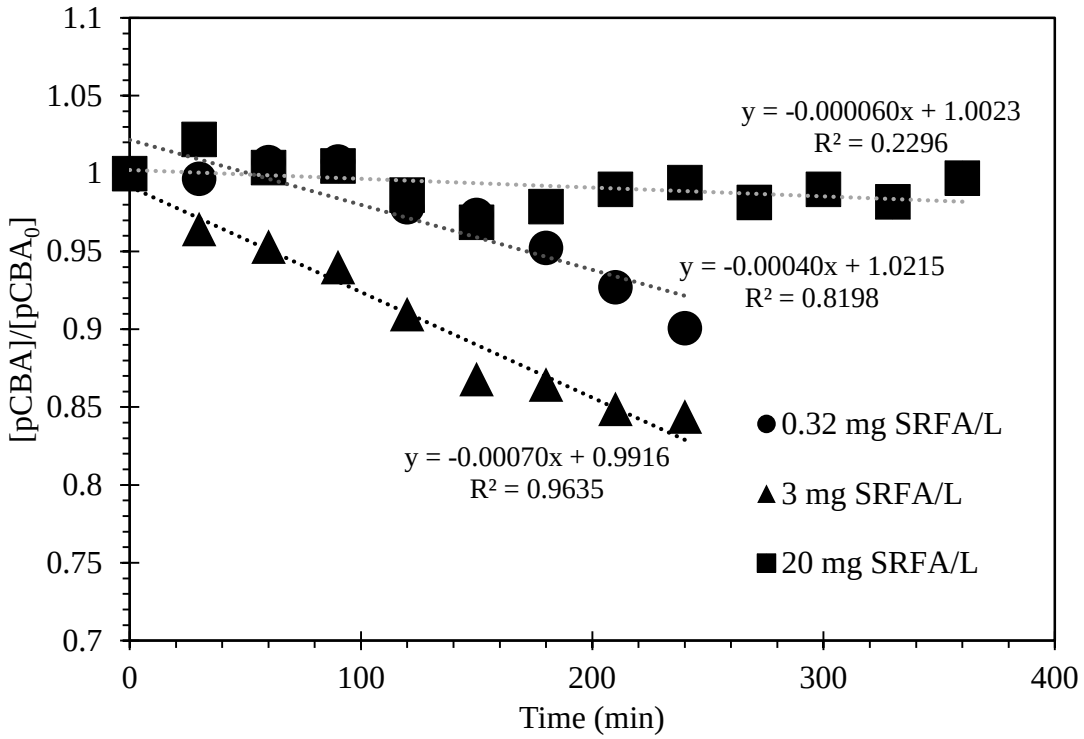

Figure 3.7. pCBA Removal in Nanopure Water Containing 0.32 ppm, 3 ppm, and 20 ppm SRFA Using a 258 nm Wavelength Cutoff Filter in Addition to AM 1.5 Global Filter

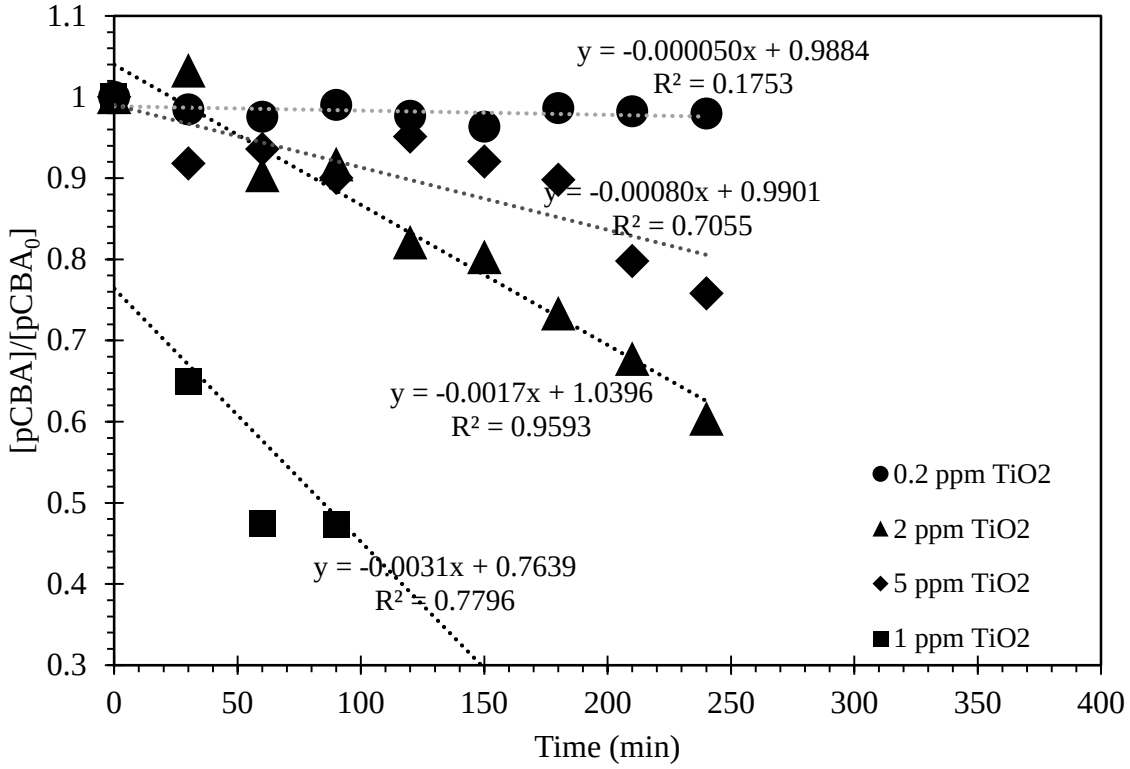

Figure 3.8. pCBA Removal in Nanopure Water Containing 0.2 ppm, 1 ppm, 2 ppm, and 5 ppm Concentrations of TiO_2 using a 258 nm Wavelength Cutoff Filter in Addition to AM 1.5 Global Filter

When pCBA levels were measured over time in the presence of 0.5 ppm and 50 ppm NO_3^- using both an AM 1.5 Global filter as well as a 258 nm cutoff filter, rate constants conformed to what was expected – pCBA levels did not change much over time for 0.5 ppm; however, the consumption of pCBA in the presence of 50 ppm NO_3^- was less than 50% after 240 minutes (Figure 3.5).

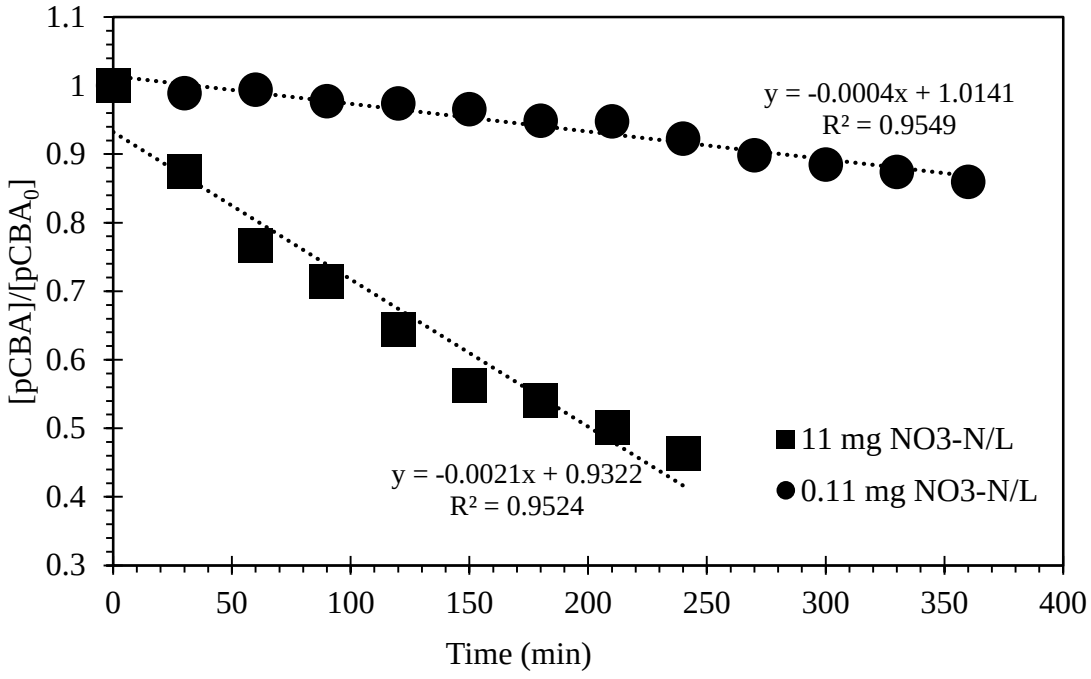

Figure 3.9. pCBA Removal in Nanopure Water Containing 0.5 ppm and 50 ppm Concentrations of $NaNO_3$ Using a 258 nm Wavelength Cutoff Filter in Addition to AM 1.5 Global Filter

Reaction rate trends

A ten-fold increase of TiO_2 from 0.2 to 2 mg/L resulted in a triple increase in pCBA. The 2 mg TiO_2/L solution was whitish in color, and higher TiO_2 concentrations remained white, but led to lower pCBA values. This could be due to light attenuation or blockage by the TiO_2. While the highest k_{pCBA} was 0.0017 min^{-1} at a concentration of 2 mg TiO_2/L, light attenuation may still have occurred at this concentration. Figure 3.6 shows the distribution of k_{pCBA} categorized by SRFA, TiO_2, and NO_3^-. Values ranged from 0.0005 to 0.0025 min^{-1}.

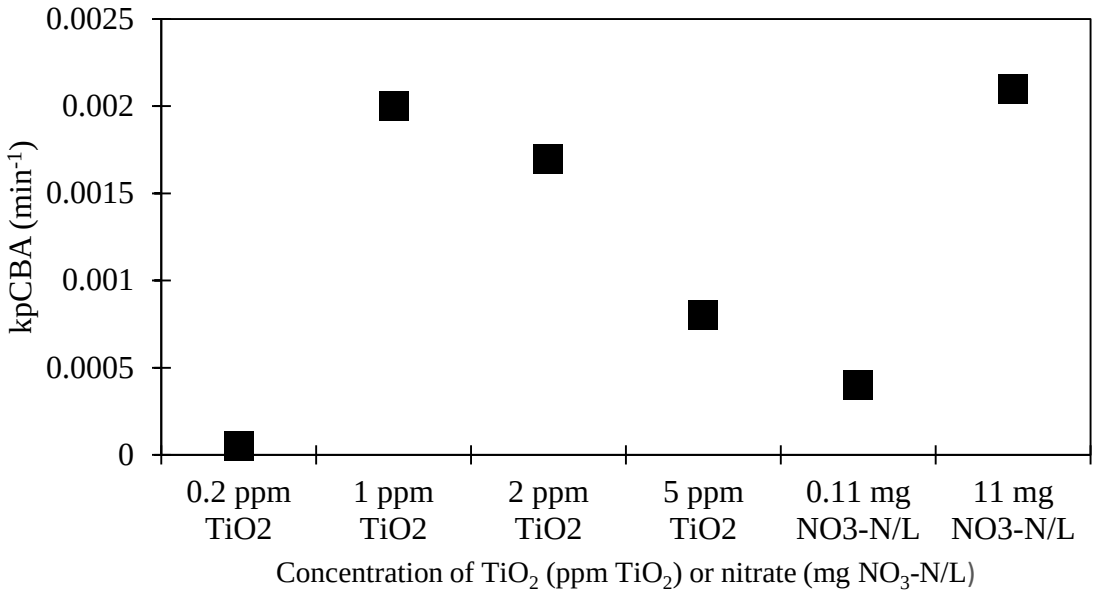

Figure 3.10. Observed Pseudo-First Order Reaction Rates for Titanium dioxide (ppm TiO_2) and Nitrate (mg NO_3-N/L) Using a 258 nm Wavelength Cutoff Filter in Addition to AM 1.5 Global Filter

To determine $[HO\cdot]_{ss}$, a kinetic model was used describing the rate change of the concentration of pCBA (equation 8), where $k_{HO/pCBA}$ is $5x10^9$ M^{-1} s^{-1}, and k_{app} is the empirically determined rate of HO·(see previous figures).[74,75]

$$\frac{d[pCBA]}{dt} = -k_{pCBA}[pCBA][HO\cdot]_{ss}$$

$$\frac{d[pCBA]}{dt} = -k_{app}[pCBA]$$

$$[HO\cdot]_{ss} = \frac{k_{app}}{k_{pCBA}} \qquad \text{(Equation 8)}$$

Figure 3.1 shows concentrations of steady state HO· calculated for each concentration of TiO_2 and NO_3^-.

Table 3.1. $[HO\cdot]_{ss}$ Concentrations for Concentrations of TiO_2 (ppm TiO_2) and NO_3^- (mg NO_3-N/L)

	Concentration (ppm TiO_2 or mg NO_3-N/L)	$[HO\cdot]_{ss}$ for TiO_2, M	$[HO\cdot]_{ss}$ for NO_3-N, M
0.2 ppm TiO_2	0.2	$1.7x10^{-16}$	
1 ppm TiO_2	1	$6.7x10^{-15}$	
2 ppm TiO_2	2	$5.7x10^{-15}$	
5 ppm TiO_2	5	$2.7x10^{-15}$	
0.11 mg NO_3-N/L	0.11		$1.37x10^{-15}$
11 mg NO_3-N/L	11		$7.0x10^{-15}$

Figure 3.11 shows how steady state concentrations of hydroxyl radical change with nitrate (mg NO_3-N/L) and titanium dioxide (ppm TiO_2). Hydroxyl radical concentration increased with concentration of both titanium dioxide and nitrate.

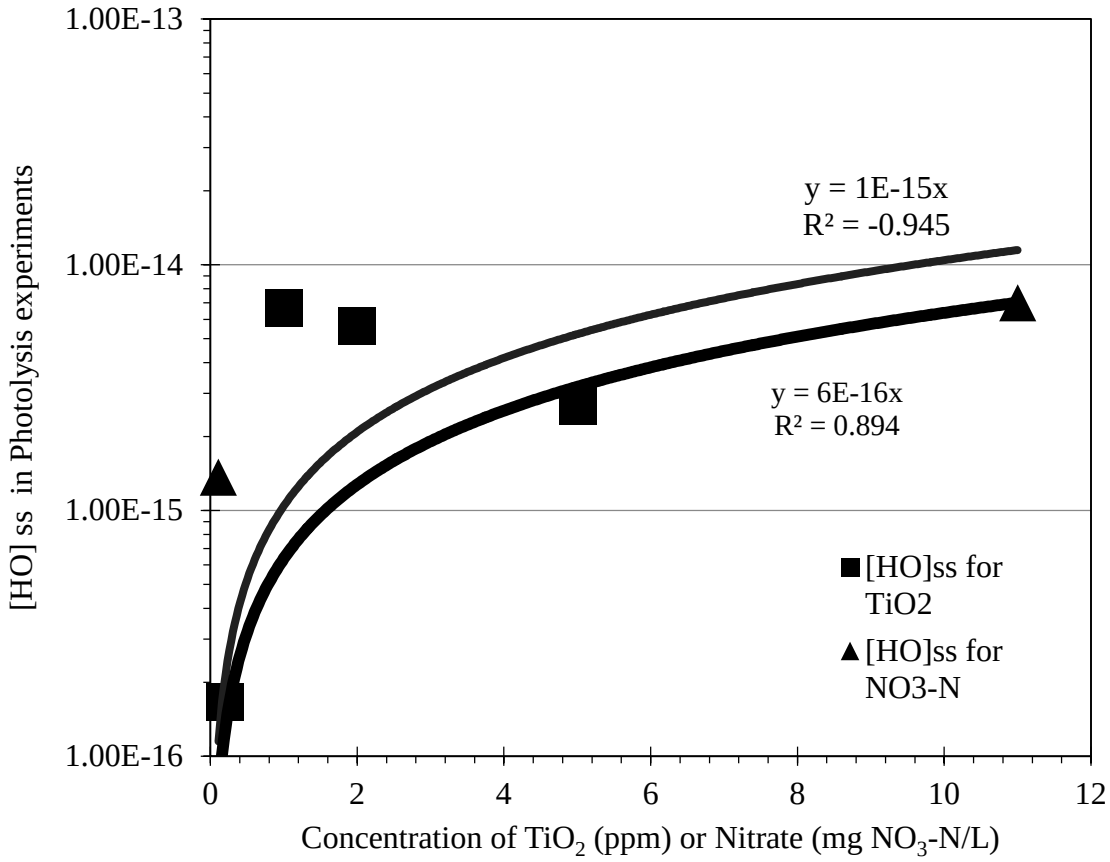

Figure 3.11. Steady-State Concentration of Hydroxyl Radical Versus Concentration of TiO_2 (ppm TiO_2) and Nitrate (mg NO_3-N/L) Using a 258 nm Wavelength Cutoff Filter in Addition to AM 1.5 Global Filter

Table 3.2 takes the empirical measurements made in this study and predicts concentrations of titanium dioxide (ppm TiO_2) and nitrate (mg NO_3-N/L) for comparison. Overall, TiO_2 concentrations need to be about 1.3 times lower than nitrate concentrations to produce the same amount of HO· in the presence of sunlight.

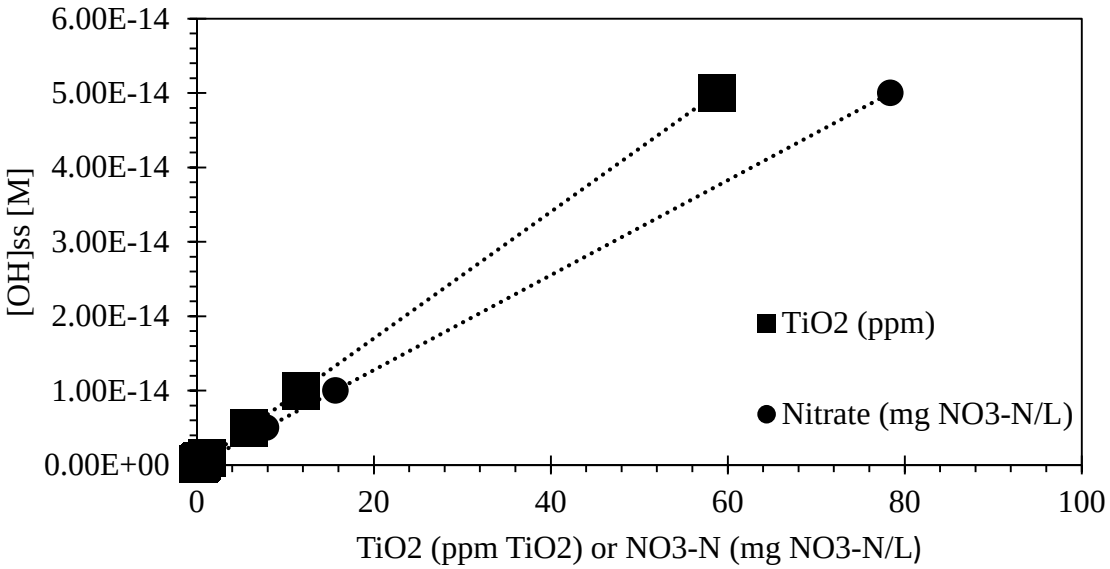

Figure 3.12. Predicted Concentrations of TiO_2 and NO_3^- Using a 258 nm Wavelength Cutoff Filter in Addition to AM 1.5 Global Filter

Measured concentrations of TiO_2 in wastewater range from 100 to 500 µg TiO_2/L.[71] Modeling has predicted TiO_2 wastewater effluent concentrations of 4 ng TiO_2/L and 5-80 µg TiO_2/L.[69,76] TiO_2 concentrations in coastal waters off of Spain were measured in the range of 32-64 µg Ti^{4+} as TiO_2/L.[77] Most of the TiO_2 concentrations used in this study are higher than those currently found or predicted in wastewater effluents. Nitrate levels in wastewater-effluent dominated rivers have shown NO_3- concentrations between 1-7 mg NO_3-N/L. Concentrations of TiO_2 that have been measured in wastewater effluents up to this point in time have been below levels of concern; however, in the case of a spill or other occurrence that would cause TiO_2 concentrations in a natural waterway to rise above 0.1 ppm, the amount of HO· produced may be an issue.

Conclusion

This study measured rates of pCBA consumption in the presence of various concentrations of Suwannee River Fulvic Acid (SRFA), TiO_2 nanoparticles, and nitrate in order to compare rates of pCBA oxidation under simulated solar light. Pseudo first order rate constants were calculated to compare concentrations of SRFA, TiO_2, and nitrate which will produce equivalent amounts of hydroxyl radicals. Steady state HO· concentration was found to increase with TiO_2 and NO_3^- concentration under simulated solar irradiation. Additionally, TiO_2 concentration would need to be 1.3 times less that of NO_3^- to produce an equivalent amount of HO· under simulated solar irradiation. These findings indicate that increasing TiO_2 loads in natural waters will have implications for hydroxyl radical concentrations, which may in turn affect ecosystem health. Further research should be designed towards experiments that are representative of TiO_2 and NO_3^- concentrations in wastewater and waste-effluent affected natural waters.

REFERENCES

(1) Huang, Z.-M.; Zhang, Y.-Z.; Kotaki, M.; Ramakrishna, S. *Compos. Sci. Technol.* **2003**, *63*, 2223–2253.

(2) Li, D.; Xia, Y. *Adv. Mater.* **2004**, *16*, 1151–1170.

(3) Caruso, R. a.; Susha, a.; Caruso, F. *Chem. Mater.* **2001**, *13*, 400–409.

(4) Bouclé, J.; Ravirajan, P.; Nelson, J. *J. Mater. Chem.* **2007**, *17*, 3141.

(5) Li, D.; Xia, Y. *Nano Lett.* **2003**, *3*, 555–560.

(6) Ding, B.; Kim, C. K.; Kim, H. Y.; Seo, M. K.; Park, S. J. Titanium dioxide nanofibers prepared by using electrospinning method. *Fibers and Polymers*, 2004, *5*, 105–109.

(7) Madani, M.; Sharifi-Sanjani, N.; Hasan-Kaviar, A.; Choghazardi, M.; Faridi-Majidi, R.; Hamouda, A. S. *Polym. Eng. Sci.* **2013**, *53*, 2407–2412.

(8) Li, Y.; Gong, J.; He, G.; Deng, Y. *Mater. Chem. Phys.* **2011**, *129*, 477–482.

(9) Su, C.; Ran, X.; Hu, J.; Shao, C. *Environ. Sci. Technol.* **2013**, *47*, 11562–11568.

(10) Deitzel, J. M.; Kleinmeyer, J.; Harris, D.; Tan, N. C. B. **2001**, *42*, 261–272.

(11) Casper, C. L.; Stephens, J. S.; Tassi, N. G.; Chase, D. B.; Rabolt, J. F. *Macromolecules* **2004**, *37*, 573–578.

(12) Medeiros, E. S.; Mattoso, L. H. C.; Offeman, R. D.; Wood, D. F.; Orts, W. J. Effect of relative humidity on the morphology of electrospun polymer fibers. *Canadian Journal of Chemistry*, 2008, *86*, 590–599.

(13) Ramakrishna, S.; Fujihara, K.; Teo, W.-E.; Lim, T.-C. *J. Eng. Fiber. Fabr.* **2008**, *3*, 46–47.

(14) Ramaseshan, R.; Sundarrajan, S.; Jose, R.; Ramakrishna, S. *J. Appl. Phys.* **2007**, *102*, 111101.

(15) Matijević, E.; Scheiner, P. *J. Colloid Interface Sci.* **1978**, *63*, 509–524.

(16) Doshi, J.; Reneker, D. H. *J. Electrostat.* **1995**, *35*, 151–160.

(17) Eda, G.; Liu, J.; Shivkumar, S. *Mater. Lett.* **2007**, *61*, 1451–1455.

(18) Lee, K. H.; Kim, H. Y.; Bang, H. J.; Jung, Y. H.; Lee, S. G. *Polymer (Guildf).* **2003**, *44*, 4029–4034.

(19) Ojha, S. S.; Afshari, M.; Kotek, R.; Gorga, R. E. *J. Appl. Polym. Sci.* **2008**, *108*, 308–319.

(20) Pai, C.-L.; Boyce, M. C.; Rutledge, G. C. *Macromolecules* **2009**, *42*, 2102–2114.

(21) Leach, M. K.; Feng, Z.-Q.; Tuck, S. J.; Corey, J. M. *J. Vis. Exp.* **2011**, 2–6.

(22) Patel, A. C.; Li, S.; Wang, C.; Zhang, W.; Wei, Y. **2007**, *120*, 12289–12296.

(23) Hendren, C. O.; Badireddy, A. R.; Casman, E.; Wiesner, M. R. *Sci. Total Environ.* **2013**, *449*, 418–425.

(24) Christian, P.; Von Der Kammer, F.; Baalousha, M.; Hofmann, T. *Ecotoxicology* **2008**, *17*, 326–343.

(25) Weir, A.; Westerhoff, P.; Fabricius, L.; Hristovski, K.; von Goetz, N. *Environ. Sci. Technol.* **2012**, *46*, 2242–2250.

(26) Klaine, S. J.; Alvarez, P. J. J.; Batley, G. E.; Fernandes, T. F.; Handy, R. D.; Lyon, D. Y.; Mahendra, S.; McLaughlin, M. J.; Lead, J. R. *Environ. Toxicol. Chem.* **2008**, *27*, 1825–1851.

(27) Mayya, K. S.; Schoeler, B.; Caruso, F. *Adv. Funct. Mater.* **2003**, *13*, 183–188.

(28) Liu, J.; Zhao, Z.; Jiang, G. *Environ. Sci. Technol.* **2008**, *42*, 6949–6954.

(29) Amirbahman, A.; Olson, T. M. *Environ. Sci. Technol.* **1993**, *27*, 2807–2813.

(30) Phenrat, T.; Song, J. E.; Cisneros, C. M.; Schoenfelder, D. P.; Tilton, R. D.; Lowry, G. V. *Environ. Sci. Technol.* **2010**, *44*, 4531–4538.

(31) Anjum, N. A.; Gill, S. S.; Duarte, A. C.; Pereira, E.; Ahmad, I. *J. Nanoparticle Res.* **2013**, *15*.

(32) Liau, S. Y.; Read, D. C.; Pugh, W. J.; Furr, J. R.; Russell, A. D. *Lett. Appl. Microbiol.* **1997**, *25*, 279–283.

(33) Ratte, H. T. *Environ. Toxicol. Chem.* **1999**, *18*, 89–108.

(34) Croteau, M. N.; Misra, S. K.; Luoma, S. N.; Valsami-Jones, E. *Environ. Sci. Technol.* **2011**, *45*, 6600–6607.

(35) Nguyen, K. C.; Seligy, V. L.; Massarsky, A.; Moon, T. W.; Rippstein, P.; Tan, J.; Tayabali, a F. *J. Phys. Conf. Ser.* **2013**, *429*, 012025.

(36) Tufenkji, N. *Adv. Water Resour.* **2007**, *30*, 1455–1469.

(37) Hermansson, M. *Colloids Surfaces B Biointerfaces* **1999**, *14*, 105–119.

(38) Song, J. E.; Phenrat, T.; Marinakos, S.; Xiao, Y.; Liu, J.; Wiesner, M. R.; Tilton, R. D.; Lowry, G. V. *Environ. Sci. Technol.* **2011**, *45*, 5988–5995.

(39) Phenrat, T.; Saleh, N.; Sirk, K.; Kim, H. J.; Tilton, R. D.; Lowry, G. V. *J. Nanoparticle Res.* **2008**, *10*, 795–814.

(40) EPA, U. Fate , Transport and Transformation Test Guidelines: OPPTS 835.1110 Activated Sludge Isotherm, 2008.

(41) Kiser, M. a.; Ladner, D. a.; Hristovski, K. D.; Westerhoff, P. K. *Environ. Sci. Technol.* **2012**, *46*, 7046–7053.

(42) Hartmann, G.; Baumgartner, T.; Schuster, M. *Anal. Chem.* **2014**, *86*, 790–796.

(43) Liu, J.; Chao, J.; Liu, R.; Tan, Z.; Yin, Y.; Wu, Y.; Jiang, G. *Anal. Chem.* **2009**, *81*, 6496–6502.

(44) Kim, H. J.; Phenrat, T.; Tilton, R. D.; Lowry, G. V. *Environ. Sci. Technol.* **2009**, *43*, 3824–3830.

(45) Phenrat, T.; Liu, Y.; Tilton, R. D.; Lowry, G. V. *Environ. Sci. Technol.* **2009**, *43*, 1507–1514.

(46) Theng, B. K. G.; Yuan, G. *Elements* **2008**, *4*, 395–399.

(47) Lin, S.; Cheng, Y.; Bobcombe, Y.; L. Jones, K.; Liu, J.; Wiesner, M. R. *Environ. Sci. Technol.* **2011**, *45*, 5209–5215.

(48) Sagee, O.; Dror, I.; Berkowitz, B. *Chemosphere* **2012**, *88*, 670–675.

(49) Cornelis, G.; Pang, L.; Doolette, C.; Kirby, J. K.; McLaughlin, M. J. *Sci. Total Environ.* **2013**, *463-464*, 120–130.

(50) Westerhoff, P. K.; Kiser, M. a.; Hristovski, K. *Environ. Eng. Sci.* **2013**, *30*, 109–117.

(51) Kaegi, R.; Voegelin, A.; Sinnet, B.; Zuleeg, S.; Hagendorfer, H.; Burkhardt, M.; Siegrist, H. *Environ. Sci. Technol.* **2011**, *45*, 3902–3908.

(52) Kiser, M. a.; Ryu, H.; Jang, H.; Hristovski, K.; Westerhoff, P. *Water Res.* **2010**, *44*, 4105–4114.

(53) Hristovski, K. D.; Westerhoff, P. K.; Posner, J. D. *J. Environ. Sci. Health. A. Tox. Hazard. Subst. Environ. Eng.* **2011**, *46*, 636–647.

(54) Blough, N. V; Zepp, R. G. In *Active Oxygen in Chemistry*; Foote, C. S.; Selverstone Valentine, J.; Greenberg, A.; Liebman, J. F., Eds.; Blackie Academic & Professional: Glasgow, 1995; pp. 280–333.

(55) Brezonik, P. L.; Fulkerson-Brekken, J. *Environ. Sci. Technol.* **1998**, *32*, 3004–3010.

(56) Canonica, S.; Kohn, T.; Mac, M.; Real, F. J.; Wirz, J.; Von Gunten, U. *Environ. Sci. Technol.* **2005**, *39*, 9182–9188.

(57) Westerhoff, P.; Aiken, G.; Amy, G.; Debroux, J. *Water Res.* **1999**, *33*, 2265–2276.

(58) Kearns, D. R. *Chem. Rev.* **1971**, *71*, 395–427.

(59) Bartosz, G. *Clin. Chim. Acta* **2006**, *368*, 53–76.

(60) Lu, C.; Song, G.; Lin, J. M. *TrAC - Trends Anal. Chem.* **2006**, *25*, 985–995.

(61) Burns, J. M.; Cooper, W. J.; Ferry, J. L.; King, D. W.; DiMento, B. P.; McNeill, K.; Miller, C. J.; Miller, W. L.; Peake, B. M.; Rusak, S. a.; Rose, A. L.; Waite, T. D. *Aquat. Sci.* **2012**, *74*, 683–734.

(62) Pi, Y.; Schumacher, J.; Jekel, M. *Ozone Sci. Eng.* **2005**, *27*, 431–436.

(63) Elovitz, M. S.; von Gunten, U. *Ozone Sci. Eng.* **1999**, *21*, 239–260.

(64) Makino, K.; Mossoba, M.; Riesz, P. *J. Phys. Chem.* **1983**, 1369–1377.

(65) Zepp, R. G.; Faust, B. C.; Holgne, J. *Environ. Sci. Technol.* **1992**, *26*, 313–319.

(66) Zafiriou, O. C.; True, M. *Geophys. Res. Lett.* **1979**, *8*.

(67) Yao, C. C. D.; Haag, W. R. *Water Res.* **1991**, *25*, 761–773.

(68) Hendren, C. O.; Mesnard, X.; Dröge, J.; Wiesner, M. R. *Environ. Sci. Technol.* **2011**, *45*, 2562–2569.

(69) Gottschalk, F.; Sonderer, T.; Scholz, R. W.; Nowack, B. *Environ. Sci. Technol.* **2009**, *43*, 9216–9222.

(70) Robichaud, C. O.; Uyar, A. L. I. E.; Darby, M. R.; Zucker, L. G.; Wiesner, M. R. **2009**, *43*, 4227–4233.

(71) Westerhoff, P.; Song, G.; Hristovski, K.; Kiser, M. a. *J. Environ. Monit.* **2011**, *13*, 1195–1203.

(72) Gondikas, A. P.; Von Der Kammer, F.; Reed, R. B.; Wagner, S.; Ranville, J. F.; Hofmann, T. *Environ. Sci. Technol.* **2014**, *48*, 5415–5422.

(73) Windler, L.; Lorenz, C.; von Goetz, N.; Hungerbühler, K.; Amberg, M.; Heuberger, M.; Nowack, B. *Environ. Sci. Technol.* **2012**, *46*, 8181–8188.

(74) Von Gunten, U. *Water Res.* **2003**, *37*, 1443–1467.

(75) Pi, Y.; Schumacher, J.; Jekel, M. *Ozone Sci. Eng.* **2005**, 431–436.

(76) Keller, A. a; Lazareva, A. *Environ. Sci. Technol. Lett.* **2013**, *1*, 65–70.

(77) Sánchez-Quiles, D.; Tovar-Sánchez, A. *Environ. Sci. Technol.* **2014**, *48*, 9037–9042.

APPENDIX A

ABSORPTION SPECTRA AND CALIBRATION CURVES FOR FUNCTIONAL ASSAYS

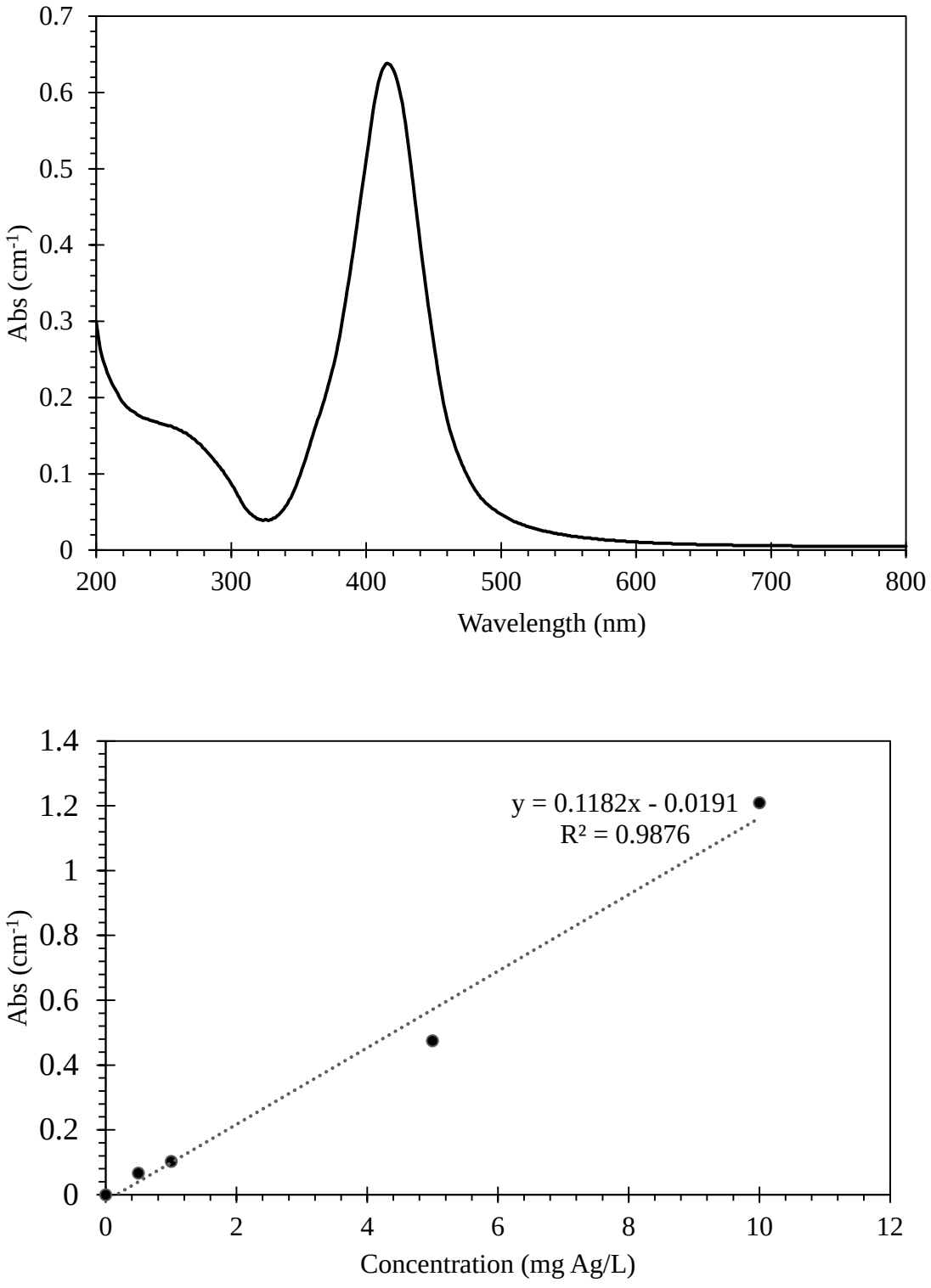

Figure A1. UV-Vis wavelength spectrum and calibration curve for PVP-AgNP.

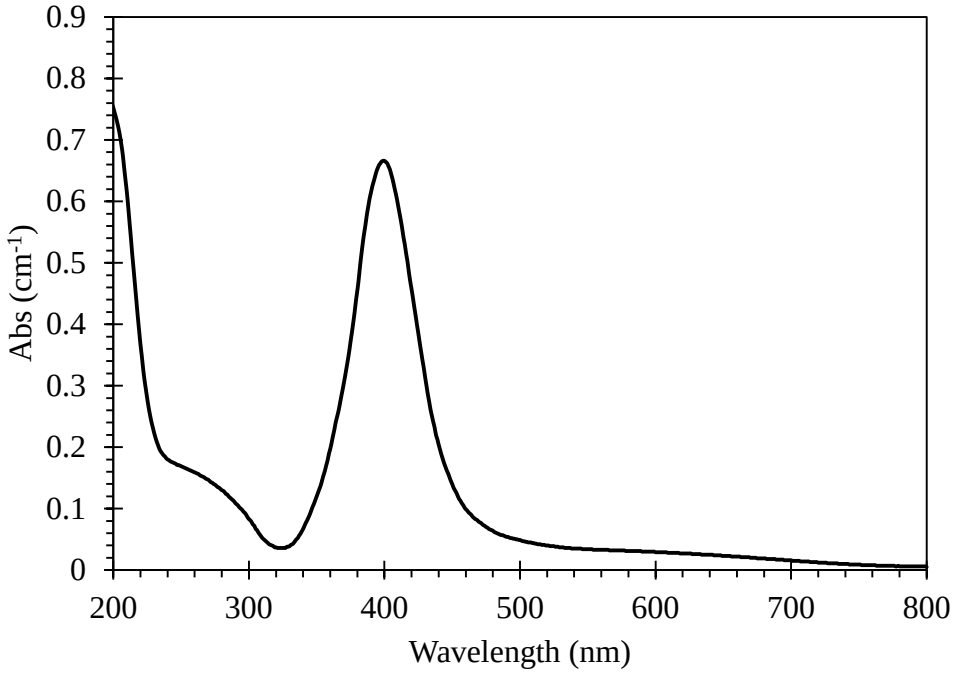

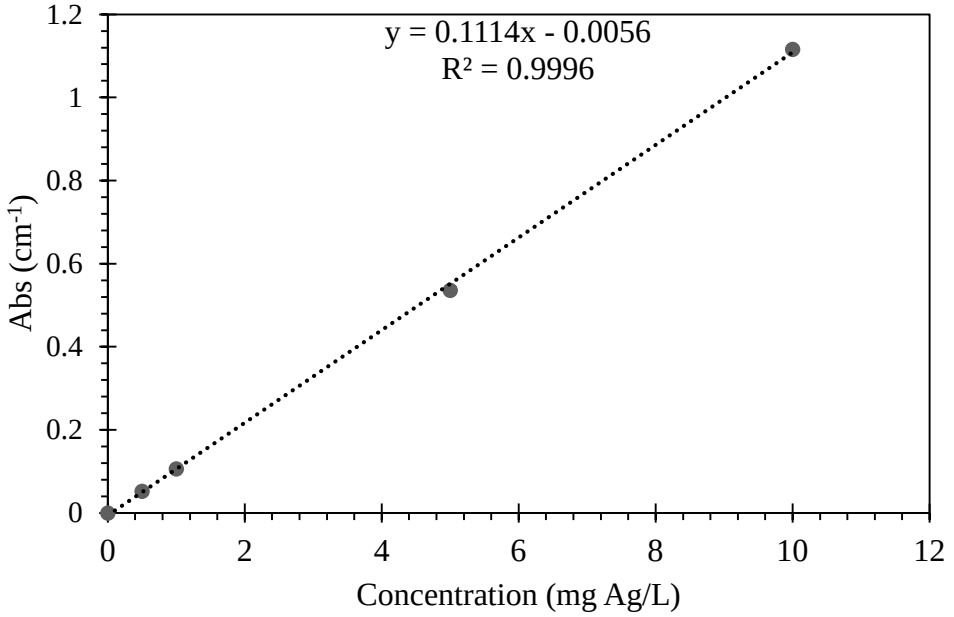

Figure A2. UV-Vis wavelength spectrum with $NaHCO_3$ buffer and without $NaHCO_3$ buffer, and calibration curve for PVP-Ag_2S-NP.

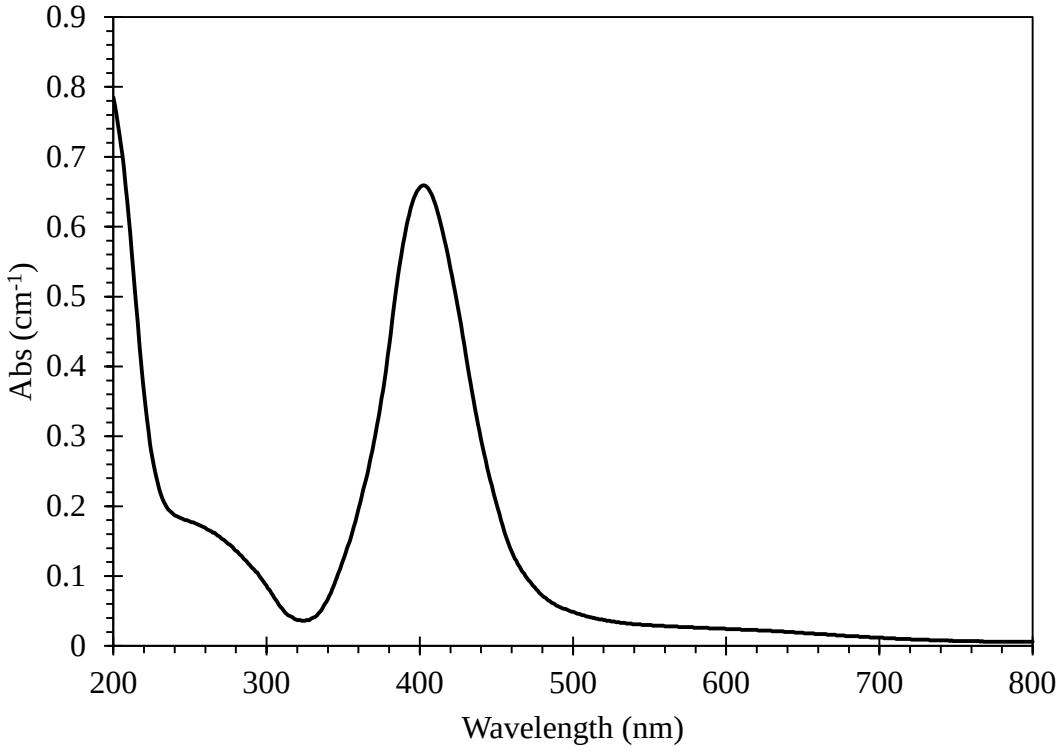

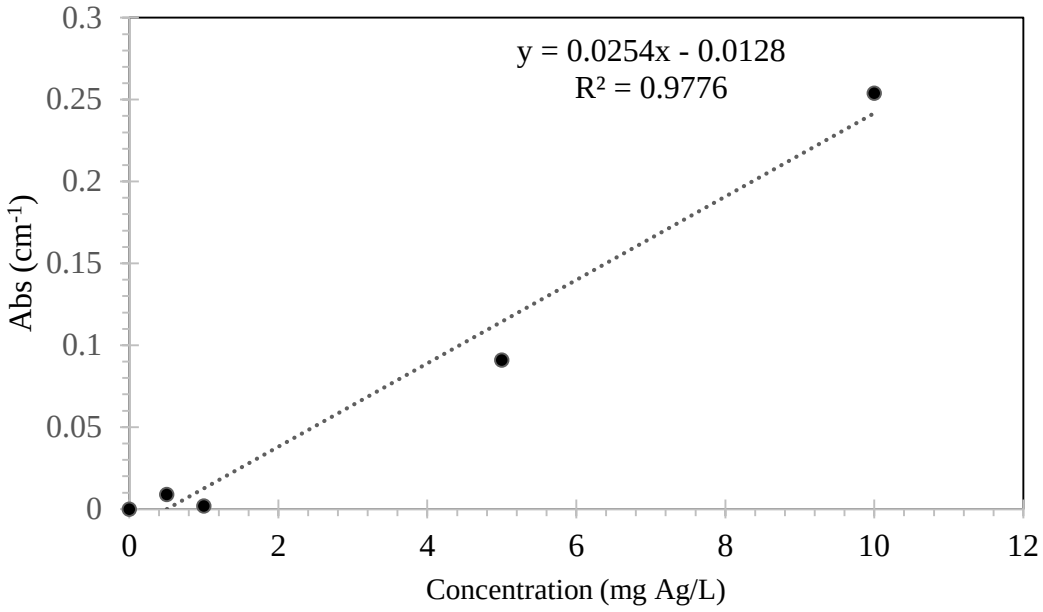

Figure A3. UV-Vis wavelength spectrum and calibration curve for Citrate-AgNP.

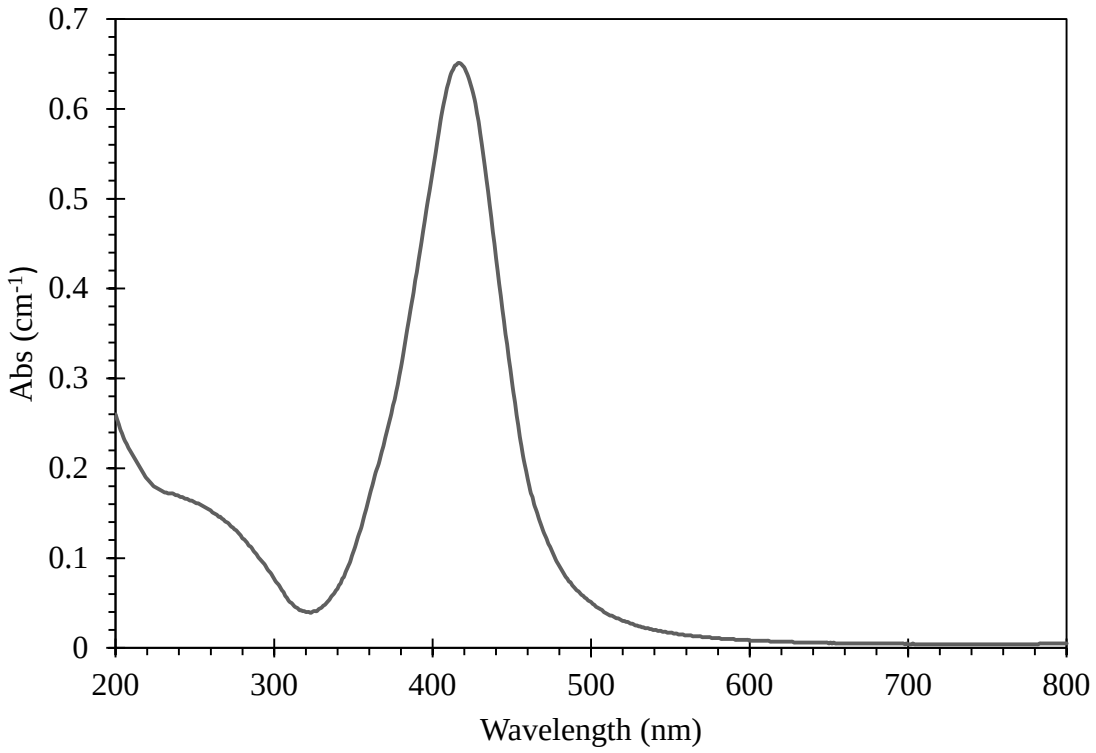

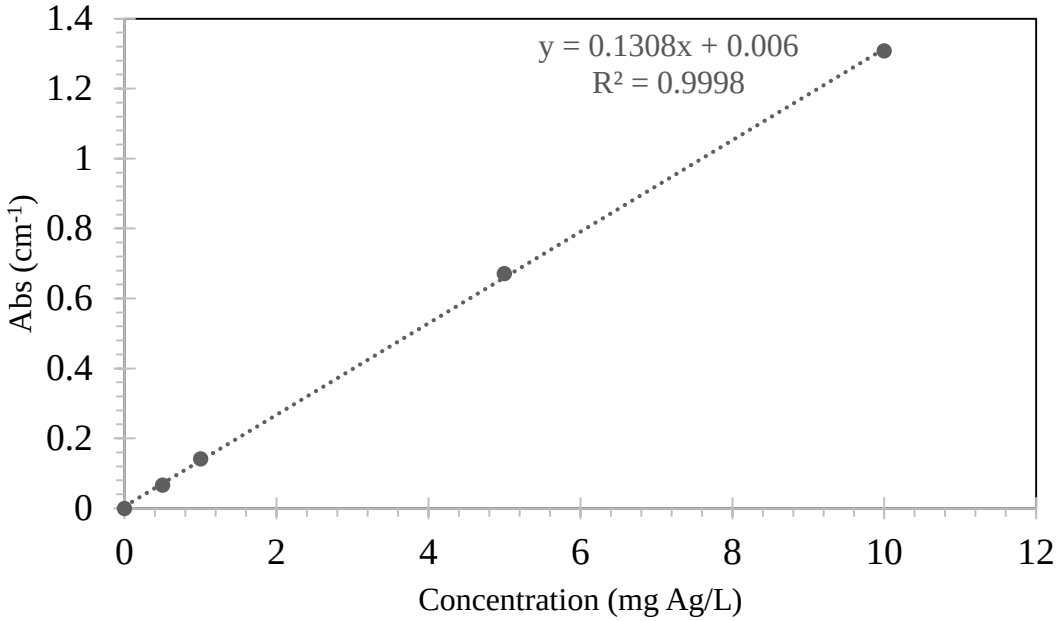

Figure A4. UV-Vis wavelength spectrum and calibration curve for Tween-AgNP.